Mesoscale Variations of the Atmospheric Snow Line over the Northern Sierra Nevada: Multiyear Statistics, Case Study, and Mechanisms

JUSTIN R. MINDER

Department of Geology and Geophysics, Yale University, New Haven, Connecticut

DAVID E. KINGSMILL

CIRES, University of Colorado, and Physical Sciences Division, NOAA/ESRL, Boulder, Colorado

ABSTRACT

Observations from several mountain ranges reveal that the height of the transition from snowfall to rainfall, the snow line, can intersect the terrain at an elevation hundreds of meters below its elevation in the free air upwind. This mesoscale lowering of the snow line affects both the accumulation of mountain snowpack and the generation of storm runoff. A unique multiyear view of this behavior based on data from profiling radars in the northern Sierra Nevada deployed as part of NOAA's Hydrometeorology Testbed is presented. Data from 3 yr of storms show that the mesoscale lowering of the snow line is a feature common to nearly all major storms, with an average snow line drop of 170 m.

The mesoscale behavior of the snow line is investigated in detail for a major storm over the northern Sierra Nevada. Comparisons of observations from sondes and profiling radars with high-resolution simulations using the Weather Research and Forecasting model (WRF) show that WRF is capable of reproducing the observed lowering of the snow line in a realistic manner. Modeling results suggest that radar profiler networks may substantially underestimate the lowering by failing to resolve horizontal snow line variations in close proximity to the mountainside. Diagnosis of model output indicates that pseudoadiabatic processes related to orographic blocking, localized cooling due to melting of orographically enhanced snowfall, and spatial variations in hydrometeor melting distance all play important roles. Simulations are surprisingly insensitive to model horizontal resolution but have important sensitivities to microphysical parameterization.

1. Introduction and background

Over major midlatitude mountain ranges with maritime climates winter storms often produce surface snowfall at high elevations and rainfall at low elevations. The elevation of the surface transition between snowfall and rainfall—the mountainside snow line—plays a central role in determining roadway navigability, river runoff, freshwater resources, and hazards from landslides, avalanches, and floods. Mountain snow line elevations, and hence the partitioning between rainfall and snowfall, are known to be sensitive to modes of interannual climate variability (e.g., Svoma 2011; Abatzoglou 2011) and show long-term trends (e.g., Knowles et al. 2006; Svoma 2009)

that have been attributed in part to anthropogenic climate change (Pierce et al. 2008). This sensitivity of the snow line to climate is the source of many of the largest climate impacts over midlatitude mountainous regions. While gross relationships between snow line elevations and temperature are known, the role of mesoscale processes in modifying the snow line on both storm and climate time scales remains poorly characterized. This study aims to improve understanding of the physical processes that determine the snow line on the mesoscale.

a. Metrics and terminology

In this study the term snow line will be used to broadly refer to the elevation in the atmosphere or at the earth's surface where falling precipitation transitions from frozen snow or graupel to liquid rain. In reality frozen hydrometeors melt over a finite time and distance, and as a result there is usually a melting layer of finite depth that contains both frozen and liquid hydrometeors. This leads

Corresponding author address: Justin R. Minder, Dept. of Atmospheric and Environmental Science, University at Albany (SUNY), 1400 Washington Avenue, Albany, NY 12222.
E-mail: jminder@albany.edu

TABLE 1. Summary of metrics used to characterize the snow line and melting layer.

Variable	Meaning	Notes
z_{0C}	Elevation of 0°C isotherm	
z_S	Elevation of mixing-ratio-based middle of melting layer	$q_f(z_S) = 0.5q_f(z_{0C})$
z_{Smin}	Elevation of mixing-ratio-based bottom of melting layer	$q_f(z_{Smin}) = 0.1q_f(z_{0C})$
z_{BB}	Elevation of peak radar brightband reflectivity	See appendix A
z_{BBmin}	Elevation of radar brightband bottom	See appendix A
D_{melt}	Characteristic frozen hydrometeor melting distance	$D_{melt} = z_{0C} - z_{Smin}$
$(D_{melt})_{BB}$	Radar brightband-based estimate of D_{melt}	$(D_{melt})_{BB} = z_{0C} - z_{BBmin}$

to a degree of ambiguity in the above definition of the snow line. For a precipitating atmosphere without inversions or isothermal layers a unique 0°C elevation z_{0C} can be defined, which marks the top of the melting layer. Beneath z_{0C} we will define two more precise measures of the snow line. The first, z_S, corresponds to the highest elevation in the melting layer where the mixing ratio of frozen hydrometeors q_f has been depleted by half relative to its value at z_{0C} [i.e., $q_f(z_S) = 0.5q_f(z_{0C})$]. This serves as a measure of the middle of the snow–rain transition zone. The second, z_{Smin}, corresponds to the highest elevation in the melting layer where q_f has been depleted by 90% relative to its value at z_{0C} [i.e., $q_f(z_{Smin}) = 0.1q_f(z_{0C})$]. This serves as a measure of the bottom of the snow–rain transition zone. The following results are only weakly sensitive to the specific fractional thresholds used to define z_S and z_{Smin}. The melting distance for frozen hydrometeors D_{melt} can be characterized as $D_{melt} = z_{0C} - z_{Smin}$.

Directly measuring z_S or z_{Smin} is difficult and often not practical. As a result we often rely on estimates of the snow line from radar remote sensing. The melting layer in stratiform precipitation often corresponds to a region of enhanced radar reflectivity referred to as the bright band (BB), caused by changes in hydrometeor fall speed, size, density, and complex index of refraction (e.g., Houze 1993; Fabry and Zawadzki 1995). The height of peak reflectivity in the BB, z_{BB}, is a useful metric characterizing the middle of the melting layer, corresponding roughly to z_S and the lowest elevation above which surface precipitation is mostly snow (White et al. 2010). The height of the BB bottom z_{BBmin} is useful as an approximate measure of the atmospheric elevation below which nearly all precipitation is liquid, corresponding roughly to z_{Smin}. A BB-based estimate of D_{melt} can be calculated as $(D_{melt})_{BB} = z_{0C} - z_{BBmin}$. The above metrics are all summarized in Table 1. Objective methods for determining z_{BB} and z_{BBmin} are discussed in section 2a and appendix A.

b. Snow lines over the northern Sierra Nevada

The northern Sierra Nevada of California (Fig. 1a) has been the site of some of the most detailed studies of the

rain–snow transition over mountains. This is a subject of importance for the region, since much of the summertime runoff comes from melting mountain snowpack and potential for flooding of mountain-fed rivers by winter storms is a substantial risk to a number of communities (including the city of Sacramento). Under projected climate warming, the increase in rain versus snow associated with rising snow lines in the Sierra is expected to increase flood risk (e.g., Das et al. 2011) and contribute to reduced summertime freshwater resources (e.g., Vicuña et al. 2007, 2011).

Classic observational work on Sierra snow lines comes from aircraft, radar, and sounding observations during the Sierra Cooperative Pilot Project (SCPP; Reynolds and Dennis 1986). More recent results come from a dense network deployed as part of the National Oceanic and Atmospheric Administration (NOAA)'s Hydrometeorology Testbed (HMT; Ralph et al. 2005) network, including surface observations and profiling radar data (discussed in detail in section 2a).

These studies have revealed that mesoscale modifications of the snow line over terrain make predicting and even characterizing the mountainside snow line over the Sierras a challenging task. For instance, in situ aircraft observations of temperature during SCPP showed z_{0C} sometimes descends by at least 400 m, relative to its upwind elevation, as air passes over the Sierras (Marwitz 1987). Furthermore, range–height indicator scans from a ground-based radar showed z_{BBmin} may descend nearly a kilometer as air rises over the windward slopes (Marwitz 1983). Similarly large descents of z_{BBmin} have been found in radar data from case studies over the windward slopes of the Italian Alps and the Oregon Cascades (Medina et al. 2005).

By examining 5 yr of data from HMT profiling radars, Lundquist et al. (2008) showed the lowering of the snow line is likely a climatological feature. Comparing hourly measurements of z_{BB} between a coastal site and a site at the foot of the Sierras revealed an average z_{BB} descent of about 100 m (Lundquist et al. 2008). The several hundred meters of mesoscale snow line lowering implied by these case studies and multiyear observations is of large enough scale to have important implications
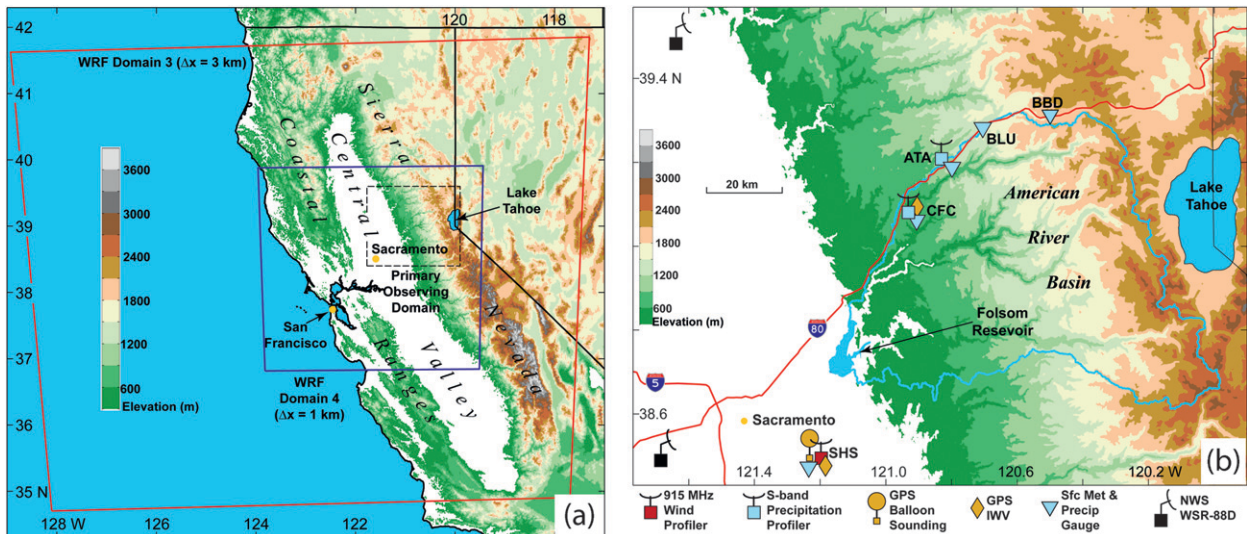
FIG. 1. Map of study area and instrumentation. (a) Topography (shading) and labels of major geographical features, as well as the boundaries of the inner two WRF domains (boxes). (b) Observational instrumentation used in the study (see legend), American River basin (blue line), and Interstates 5 and 80 (red lines).

for both hydrometeorological forecasting (e.g., White et al. 2002) and climate impacts associated with snow-pack accumulation (e.g., Minder 2010).

The ability of numerical models to capture and predict this mesoscale structure of the snow line is largely uncharacterized. A range of studies have examined the ability of mesoscale models to predict precipitation amounts over the Sierra, generally finding significant overprediction (e.g., Jankov et al. 2009; White et al. 2010; Caldwell 2010). However, these studies have not examined model skill at prediction of the spatial distribution of precipitation phase. White et al. (2010) used radar profiler measurements to evaluate the skill of California–Nevada River Forecast Center forecasts of z_{0C}. These forecasts were derived from coarse-resolution global forecasts that would not be expected to resolve mesoscale variations. They found that errors of around ±200 m are common, and occasional larger errors of 400–800 m can occur (usually underpredictions), with significant consequences for hydrological predictions (White et al. 2010).

c. Mechanisms for mesoscale snow linedrops

Informed prediction and characterization of meso-scale snow line behavior over the Sierra Nevada and elsewhere requires an understanding of the responsible physical mechanisms. Marwitz (1983, 1987) hypothesized that the absorption of latent heat by melting of oro-graphically enhanced snowfall over the windward slopes leads to localized cooling of the air, bringing snow to lower elevations. The importance of melting-induced

cooling can be inferred from soundings with 0°C iso-thermal layers (Findeisen 1940). Aircraft soundings over the Central Valley and Sierra foothills have shown approximately 200-m-thick isothermal layers atop the BB (Stewart et al. 1984; Marwitz 1983), and for one storm a survey of surface temperatures along Highway 80 (Fig. 1b) revealed an approximately 1-km-deep iso-thermal layer (Marwitz 1987).

Other mechanisms may also play important roles. Marwitz (1987) suggested that adiabatic cooling of stratified air due to orographic lifting could be partially responsible for the lowering of z_{0C}. Terrain blocking or along-barrier transport of cold prefrontal air (Parish 1982) could also play a role in maintaining colder temperatures and lower snow lines along the mountainside. Additionally, spatial variations in hydrometeor sizes or fall speeds due to orographic forcing could produce variations in the melting distance of frozen hydrometeors, causing snow line elevations to vary, independent of variations in z_{0C} (Minder et al. 2011).

Minder et al. (2011) used semi-idealized numerical simulations to diagnose and quantify the contributions of spatial variations in melting-induced cooling, adia-batic cooling, and hydrometeor melting distance. For a range of atmospheric conditions and mountain sizes, they found that all three of these mechanisms contrib-uted significantly. Questions remain about the applica-bility of Minder et al. (2011)'s results to real storms over ranges such as the Sierra Nevada, since their idealized simulations neglected potentially important processes such as surface fluxes, synoptic-scale forcing, and fully three-dimensional airflow dynamics.

d. Approach

This paper examines the mesoscale behavior of the atmospheric snow line over the Sierra Nevada and the responsible physical mechanisms. This is accomplished through the assembly of statistics from 3 yr of snow line behavior and detailed analysis of a case study. Central questions include the following:

- What mesoscale modifications of the snow line are typical?
- Do mesoscale models capture the behavior of the snow line?
- What processes cause mesoscale descent of the snow line?

Section 2 describes the observational datasets and model used in this study. Section 3 presents 3 yr of statistics on the mesoscale descent of the snow line from profiling radars. Section 4 presents a detailed case study of the snow line during a major storm, using both observations and a numerical model. The physical processes responsible for modifying the snow line on the mesoscale are diagnosed and quantified in section 5. Key sensitivities of the model are explored in section 6. Discussion and conclusions are given in section 7.

2. Methods

a. Mesoscale observations

NOAA's HMT conducts research on precipitation and weather conditions that can lead to flooding, and fosters transition of scientific advances and new tools into forecasting operations (Ralph et al. 2005; hmt.noaa.gov). HMT's first regional demonstration, HMT-West, has deployed an extensive network of instrumentation in northern California since 2003, with an emphasis on the American River basin of the northern Sierra Nevada since 2005 (Fig. 1). These observations have provided detailed documentation of airflow, precipitation, and hydrology associated with extratropical cyclones making landfall in northern California. Unlike typical field campaigns that span only a few months of a single year, observations from HMT-West span the entire cool season (approximately October–May) of several years, thus providing a unique sampling of the range of behavior found in dozens of storms. In the present study we exploit HMT-West observations to produce multiyear statistics of snow line behavior and to conduct a detailed case-study analysis.

The most essential observations for this study come from profiling Doppler radars arranged in a southwest–northeast transect from the Central Valley of California to about halfway up the western slopes of the Sierra (Fig. 1b). Two S-band (2.875 GHz) precipitation

TABLE 2. Station abbreviations, elevations, and instrumentation used in this study.

Station	Elevation (m MSL)	Instrumentation
SHS	50	915-MHz profiler, sondes, GPS IWV, 2-m temperature, surface precipitation
CFC	636	S-band profiler, GPS IWV, 2-m temperature, surface precipitation
ATA	1085	S-band profiler, 2-m temperature, surface precipitation
BLU	1610	2-m temperature, surface precipitation
BBD	1739	2-m temperature, surface precipitation

profilers (White et al. 2000) were deployed on the windward slope: one at Alta (ATA, 1085 m MSL) and another at Colfax Water (CFC, 636 m MSL). These instruments provide vertical profiles of Doppler vertical velocity V_r (positive downward) and range-corrected signal-to-noise ratio (SNR), the latter of which is converted into equivalent radar reflectivity factor Z_e. These data are collected every 1 min at a range resolution of 60 m. In addition, a 915-MHz radar wind profiler (Carter et al. 1995) was deployed upwind of the Sierra, in the Central Valley at Sloughhouse (SHS, 50 m MSL). It transmits a sequence of beams that switch between different range resolutions (63 and 106 m) and different pointing angles (vertical and off vertical by about 24° in two orthogonal azimuthal directions). This sequence repeats about every 5 min. Each beam provides profiles of radial velocity and SNR. These data are used to derive vertical profiles of horizontal wind every hour that are subsequently edited objectively using the methods of Weber et al. (1993). We use the methods described in appendix A to objectively identify z_{BBmin} and z_{BB} in the profiler data from SHS, ATA, and CFC.

Other HMT-West observations used in this study include special balloon soundings launched from SHS, which provide measurements of z_{0C} just upwind of the terrain. Also, measurements of integrated water vapor (IWV) in the full atmospheric column above dual-frequency GPS receivers installed at SHS and CFC are retrieved at 30-min intervals (e.g., Duan et al. 1996; Mattioli et al. 2007). Finally, surface observations of temperature and precipitation are collected at SHS, CFC, ATA, Blue Canyon (BLU, 1610 m MSL), and Big Bend (BBD, 1739 m MSL). The above sources of observational data are summarized in Table 2.

b. Mesoscale model

For a selected case study a numerical simulation is conducted using version 3.2.1 of the Weather Research and Forecasting model (WRF) (Skamarock et al. 2008; http://www.mmm.ucar.edu/wrf/users/). The model is
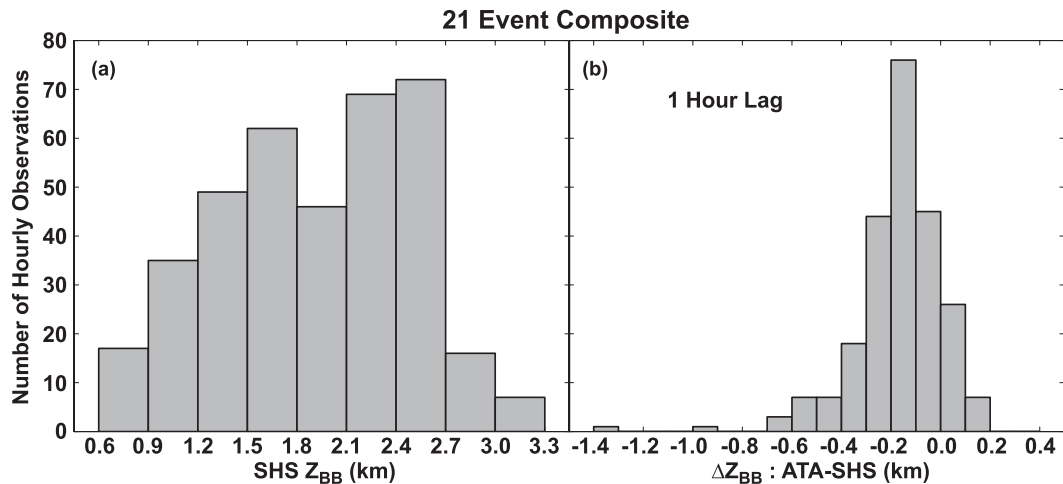
FIG. 2. Event-based z_{BB} climatology from major storms during three cold seasons (2005/06, 2006/07, and 2007/08). (a) Histogram of hourly z_{BB} at SHS. (b) Histogram of hourly Δz_{BB} between SHS and ATA (locations in Fig. 1b).

configured with four two-way nested domains centered on the northern Sierra Nevada, with horizontal grid spacing of 27, 9, 3, and 1 km and time steps of 24, 8, 4, and 2 s. The boundaries of the inner-two WRF domains are shown in Fig. 1a. A terrain-following coordinate is used with 118 unevenly spaced levels. Fine vertical spacing of 40–52 m (increasing approximately linearly with height) is used below 2.75 km to resolve vertical variations in the atmospheric snow line and z_{0C}. Above this, the vertical grid spacing increases to 340 m at the base of the damping layer and 740 m at the model top. Model output is written to disk every 30 min of model time for analysis (although limited 2-min output is used for the trajectory analysis in section 5a).

The simulations are driven with initial and boundary conditions from the North American Regional Reanalysis (NARR). On the outer two coarse WRF grids the solution is nudged toward the NARR grids to maintain synoptic-scale circulation close to that observed. No nudging is applied on the inner two grids. Third-order Runge–Kutta time stepping is used, with fifth-order horizontal and third-order vertical advection. A positive-definite limiter is applied during the advection of microphysical variables (Skamarock and Weisman 2009). The upper-boundary condition is a constant pressure surface, with the vertical velocity damping layer described by Klemp et al. (2008) applied above about 9.5 km MSL to prevent the reflection of gravity waves off the model top.

Longwave and shortwave radiative fluxes are parameterized with the Rapid Radiative Transfer Model (Mlawer et al. 1997) and Dudhia schemes (Dudhia 1989). On the outer three domains, convection is parameterized with the Kain–Fritsch scheme (Kain 2004), while only explicitly simulated convection is considered on the 1-km

grid. Subgrid-scale turbulence is parameterized using the Mellor–Yamada–Janjic scheme (Mellor and Yamada 1982; Janjic 2002). The surface layer is parameterized using the Eta scheme (Janjic 1996). The land surface is parameterized using the Noah land surface model (Chen and Dudhia 2001).

Cloud and precipitation microphysics are parameterized with the WRF single-moment six-class (WSM6) scheme (Hong et al. 2004; Hong and Lim 2006)—a single-moment bulk scheme that predicts the mixing ratios of water vapor, cloud water, cloud ice, rain, snow, and graupel. It was chosen based on its performance in simulating the case and its intermediate complexity relative to the other schemes in WRF, which made some of the diagnostics in section 4 more straightforward. In WSM6, melting of snow and graupel is parameterized following Rutledge and Hobbs (1983). This parameterization neglects the effects of vapor transfer on the heat balance of melting hydrometeors. In the near-saturated melting layer studied here (simulated RH > 99%), such a scheme is expected to underestimate melting rates (e.g., Szyrmer and Zawadzki 1999), and hence overestimate D_{melt}. A cloud droplet number concentration of 100 cm^{-3} is prescribed, representative of relatively clean maritime air. To allow for comparison with profiler observations, WRF output is used to calculate profiles of Z_e and V_r, as well as z_{BBmin} (as described in appendix B).

3. Multiyear statistics

To characterize the mesoscale behavior of the snow line over the northern Sierra, radar profilers are used to develop multiyear statistics of the spatial variations in z_{BB} between the upwind Central Valley (at SHS) and

the windward slopes (at ATA). We focus on the cool seasons of 2005/06, 2006/07, and 2007/08, when profilers were installed at both SHS and ATA. For each of these seasons, the seven largest precipitation-producing events (based on precipitation gauge data at BLU) that had z_{BB} data from both SHS and ATA are identified. The number of events per season is chosen to equal the number of qualifying events from the season with the fewest (2006/07). The average event duration was 47 h and the average event liquid-equivalent precipitation accumulation at BLU was 97 mm. Hourly z_{BB} values are derived at SHS and ATA. For hours with successful z_{BB} retrievals from both SHS and ATA, the difference in z_{BB} between the two sites is calculated as $\Delta z_{BB} = (z_{BB})_{ATA} - (z_{BB})_{SHS}$. This procedure is repeated with SHS z_{BB} data shifted forward by 1 and 2 h to test the sensitivity of results to the estimated advection/propagation time between the sites.

A histogram of hourly z_{BB} at SHS is shown in Fig. 2a. These 21 events display a wide range of upwind z_{BB}, with some elevations on the lower windward Sierra slope, while others are above 2.7 km MSL of the Sierra crest. Since most values of z_{BB} are at or below crest height but above mountain base, mesoscale variations in z_{BB} may act to influence the accumulation of snowfall and the timing of runoff.

Hourly values of Δz_{BB} (with a 1-h SHS shift) reveal that a mesoscale lowering of z_{BB} over the windward Sierra slope is a consistent feature, as Δz_{BB} is negative for 86% of samples (Fig. 2b). This is only weakly sensitive to choice of SHS shift (80% for 0 h, 83% for 2 h). While the mode of the distribution is 100–200 m of lowering, there is significant variability, with several samples each showing over 600 m of lowering. The mean Δz_{BB} over all samples is 170 m (150 m for 0-h SHS shift, 170 m for 2 h). Broadly similar results were found when 2 yr of available data from CFC were analyzed. This mean lowering is larger than the 100 m of z_{BB} reported by Lundquist et al. (2008). However, their study compared a profiler site on the Pacific coast with a site at the base of the Sierra. Accordingly, their derived z_{BB} values could differ from those found in the present study owing to airmass transformation over the Coast Range and modifications of z_{BB} directly over the Sierra windward slope.

This persistent lowering of z_{BB}, and presumably the snow line, during major Sierra storms argues for the importance of mesoscale snow line modifications for the climatology of mountain snow accumulation. This result, and the observed variability in Δz_{BB}, highlights the importance of considering mesoscale snow line variations in hydrologic forecasting. Motivated by these results, we now examine a case study in order to diagnose
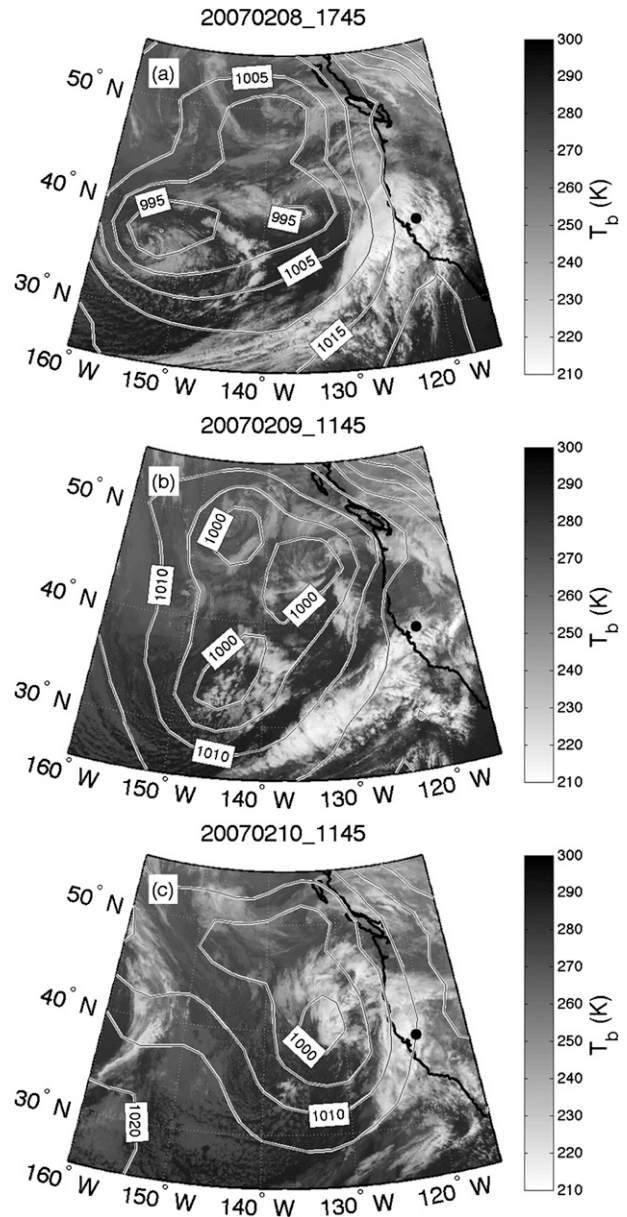

FIG. 3. Sequence of GOES-West infrared images and NARR SLP showing the synoptic evolution of the case-study event. GOES brightness temperatures T_b are shown in grayscale according to the color bar. NARR SLP is contoured every 5 hPa. The times for GOES images are denoted above each frame (formatted as yyyymmdd_HHMM UTC). The NARR SLP is from 15 min later than the labeled time. Black dot shows the location of SHS.

the causes of snow line lowering and to evaluate the ability of numerical models to capture this behavior.

4. Case study: 8–12 February 2007

We focus here on examining the mesoscale behavior of the snow line during 8–12 February 2007. This event is chosen in part for its hydrologic significance: it
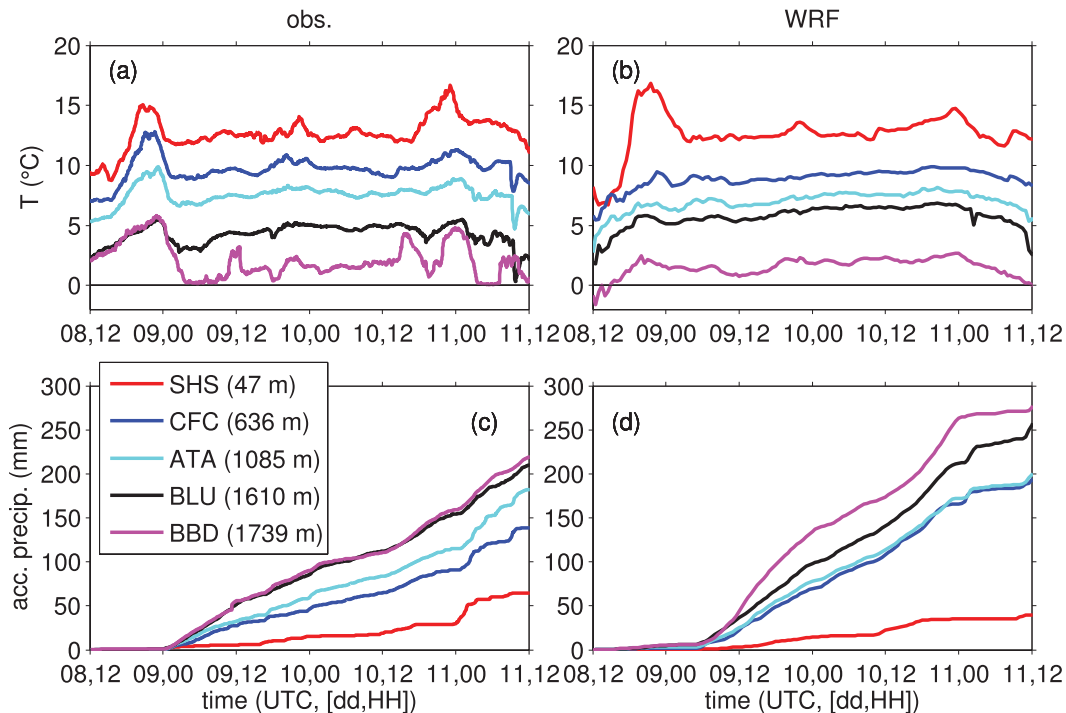
FIG. 4. Surface temperature and accumulated precipitation from observations and WRF for sites labeled in Fig. 1 (station elevations denoted in meters MSL). Colored lines denote different stations as indicated in legend. (a) Observed 2-m temperature. (b) WRF-simulated 2-m temperature. (c) Observed accumulated precipitation. (d) WRF-simulated accumulated precipitation. WRF time series come from the nearest grid point to each station location. A 6.5°C km^{-1} lapse rate correction has been applied to the WRF temperature time series to account for differences between gridpoint and station observations.

produced the largest precipitation totals of the water year at a number of northern Sierra locations. It is also chosen as representative of mesoscale snow line variations, since the average Δz_{BB} for this event is similar to the median value from the above multiyear statistics. Finally, this event is chosen because of its long duration and relatively steady conditions in terms of z_{BB}, which helps to simplify the subsequent analysis.

a. Observational results

During 8–12 February 2007 two extratropical cyclones impacted northern California in close succession, producing continuous snowfall and rainfall over the northern Sierra Nevada for over 72 h. Figures 3a–c provide a synoptic context for the event from Geostationary Operational Environmental Satellite-West (GOES-West) IR imagery and NARR sea level pressure (SLP). Figures 4a,c show 2-m temperature and accumulated precipitation over the event for a transect of stations over the windward slope denoted in Fig. 1.

At 1745 UTC 8 February the low pressure center of an occluded cyclone is located to the west of northern California, while frontal clouds from the cyclone have begun to cover the northern Sierra, and geostrophic south-southwesterly flow impinges on the terrain (Fig. 3a). Surface observations around this time show no precipitation but warming associated with the approaching front (Figs. 4a,c). At about 0900 UTC 9 February, heavy precipitation begins at surface stations in the northern Sierra, with substantial orographic enhancement (Fig. 4c). This is initially accompanied by cooling across the transect (Fig. 4a) because of subcloud evaporation in the prefrontal air mass.

As the low pressure center tracks northward, south-southwesterly flow, frontal clouds, and rainfall continue over northern California (Fig. 3b). From about 0600 UTC 9 February to 1600 UTC 10 February, surface precipitation is continuous and temperatures are nearly constant at low- and midelevation stations. Of the stations included in the transect, only BBD has temperatures that approach 0°C, and it is the only station receiving snow, showing that the snow line is relatively high in the warm air associated with this storm. By 1145 UTC 10 February, a second cyclone is affecting the region, providing continued synoptic forcing and south-southwesterly flow (Fig. 3c). At around 0000 UTC 11 February the cold
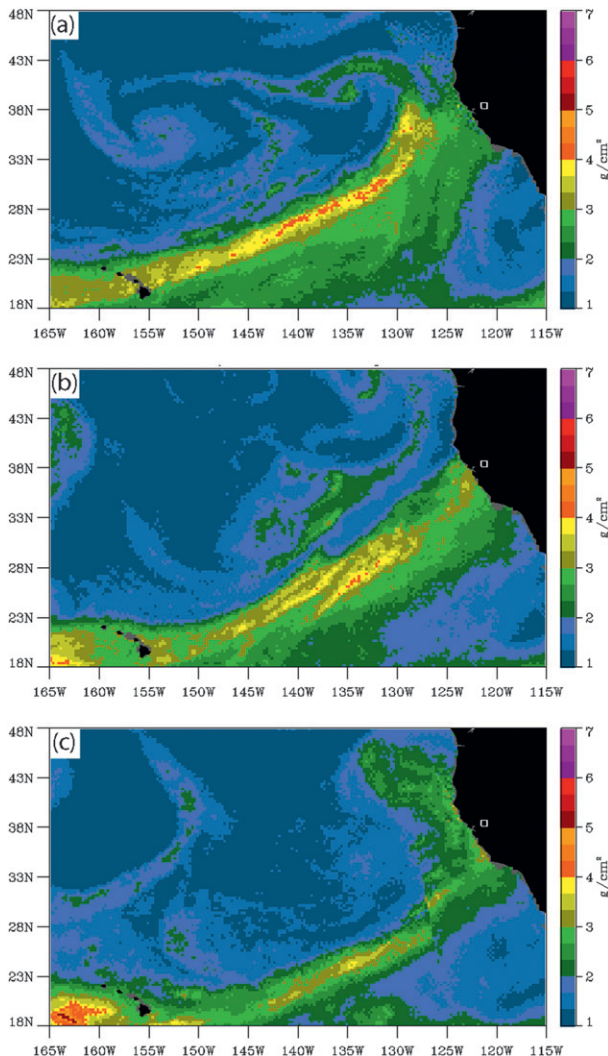
FIG. 5. Vertically integrated water vapor composited from SSM/I retrievals. (a) 1200–2400 UTC 8 Feb, (b) 1200–2400 UTC 9 Feb, and (c) 1200–2400 UTC 10 Feb. White square denotes the location of SHS.

front associated with this cyclone passes over the region, producing the heaviest recorded rainfall rates, and cooling across the station transect (Figs. 4a,c).

A sequence of maps of vertically integrated water vapor (IWV) including times just before and during the major precipitation is shown in Fig. 5. These are constructed by compositing measurements from a constellation of polar-orbiting satellites carrying the Special Sensor Microwave Imager (SSM/I) sensors, using the algorithm of Wentz (1995) over 12-h periods. They show a plume of moisture extending from the subtropics to the California coast, elongated along the southwesterly flow, which persists throughout the event. When lifted over terrain, such "atmospheric rivers" of water vapor flux are the typical moisture source for heavy rainfall

and snowfall events over the coastal mountains of western North America (e.g., Neiman et al. 2008; Guan et al. 2010).

Focusing on the mesoscale structures of this event, Fig. 6 shows data from wind profiler and balloon sounding measurements at SHS, just upwind of the Sierra. Before the beginning of rainfall (1200–2400 UTC 8 February) low-level winds are weak and south-southeasterly (Figs. 6a,b). However, the approaching warm front is apparent aloft, with a region of strong veering winds descending toward the surface over time. The front is also apparent in the balloon soundings as high–equivalent potential temperature (θ_e) air descends from aloft and the water vapor mixing ratio q_v increases at midlevels (Figs. 6c,d). GPS measurements of IWV at SHS and CFC reveal increasing IWV associated with the warm-frontal passage (Fig. 6e), which is maintained throughout the storm by the supply of moisture from the atmospheric river. The cold-frontal passage that marks the event's end is apparent from 0000 to 1200 UTC 11 February. During this time θ_e and IWV decrease, and low-level winds veer to WSW. Between frontal passages, z_{0C} at SHS was remarkably steady, varying only 100–200 m.

Between the major frontal passages there is significant directional shear between southwesterly flow aloft and low-level along-barrier southeasterly flow. Around 500 m MSL there is often a local maximum of along-barrier winds ($\sim$15 m s^{-1}). This feature is known as the Sierra barrier jet (SBJ; Parish 1982). It is a manifestation of terrain-blocked airflow that is typical of Sierra storms and plays an important role in redistributing water vapor and precipitation (e.g., Smith et al. 2010; Neiman et al. 2010; Lundquist et al. 2010). The height and strength of the SBJ in this case is typical of those found in multiyear statistics (e.g., Neiman et al. 2010).

The vertical structure of precipitation over the windward slopes is shown in detail by the S-band profiler at CFC (Fig. 7a). As the warm front approaches, echoes aloft show virga. These give way to deep and intense stratiform echoes as the surface front reaches the Sierra. Throughout the storm there are significant variations in echo depth and intensity. These occur on time scales of several hours (likely owing to variations in synoptic forcing and vapor supply) and on time scales of tens of minutes (likely owing to embedded convection). The deepest and most intense echoes are associated with the cold-frontal passage just after 0000 UTC 11 February, during and after which the echoes have a more convective form. Throughout most of the storm a radar BB is apparent in the S-band data (z_{BBmin} is plotted as a thin line in Fig. 7a). However, at times there is no distinct BB, despite significant surface rainfall (e.g., 0600–1600 UTC
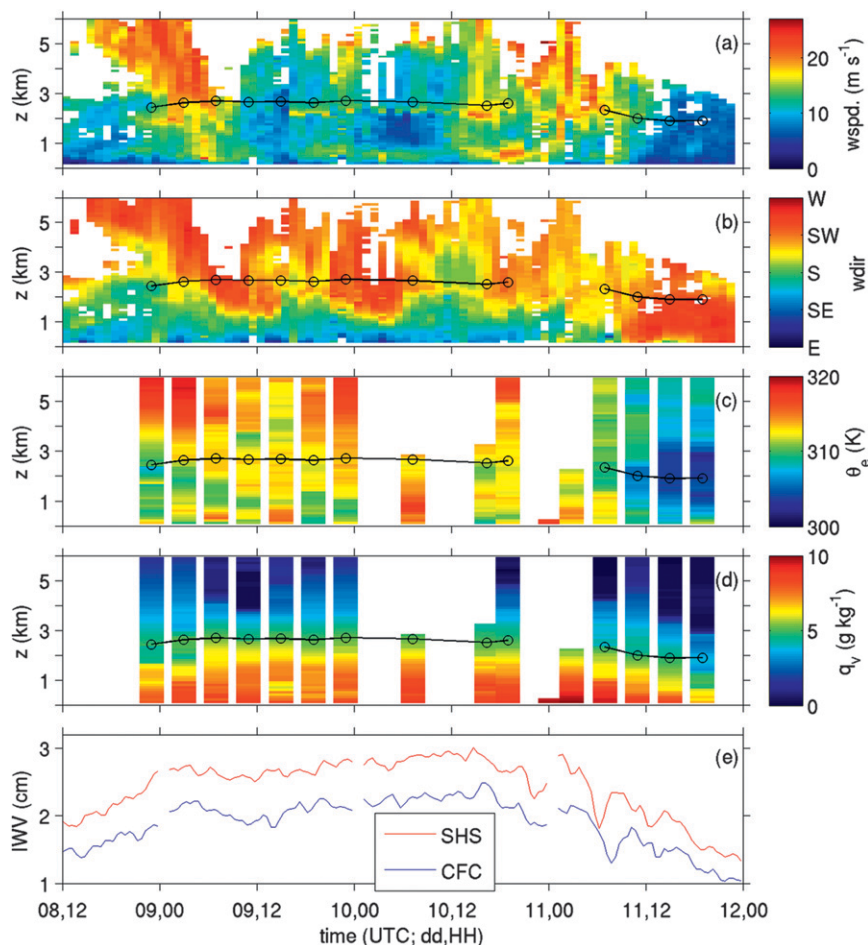
FIG. 6. Upwind time–height sections at SHS. (a),(b) Wind speed and direction from the 915-MHz wind profiler with color shading. (c),(d) θ_e and q_v from balloon soundings with color shading. These are represented with 3-h-wide color-shaded bars, centered on the sounding time. All panels show z_{0C} deduced from balloon soundings with open circles connected by black lines. (e) GPS-derived measurements of IWV at SHS and CFC.

9 February). This non-BB (NBB) rain is likely indicative of shallow precipitation forced by orographic ascent of moist air without substantial seeding ice from aloft (e.g., White et al. 2003; Neiman et al. 2005). This general sequence of vertical echo structures appears to be typical of landfalling cyclones over mountainous terrain (e.g., Medina et al. 2007).

Spatial variations of the snow line are examined in Fig. 8a by plotting time series of z_{BBmin} from the three radar profilers, along with z_{0C} from SHS balloon soundings. The data from SHS is shifted forward by 1 h in this plot and subsequent statistics to roughly account for advection time between the sites. We choose this value of shift since it maximizes the correlation between z_{BBmin} at SHS and CFC while corresponding to physically reasonable windspeeds ($\sim$20 m s^{-1}). At SHS, precipitation is intermittent, and consequently there are

fewer retrievals of z_{BBmin} as compared to the mountain sites. As expected, z_{BBmin} at SHS is consistently displaced below z_{0C} because of the finite time it takes for hydrometeors to melt as they fall. This displacement is thus a measure of the melting distance of frozen hydrometeors and typically ranges from about 100–300 m at SHS. At all sites the snow line reacts to the frontal passages, with z_{BBmin} rising during the initial warm front, and descending with the cold front. There is a fairly consistent spatial variation in z_{BBmin}, with the mountain sites (CFC, ATA) showing lower z_{BBmin} than the upwind site (SHS). This is quantified by averaging the difference between z_{BBmin} at SHS and each mountain site over all times with coincident measurements (see Δz_{BBmin}, Table 1). The value of Δz_{BBmin} is 123 m at CFC and 150 m at ATA, showing a descent of the BB toward the terrain that is comparable with typical storm-averaged values (Fig. 2b).
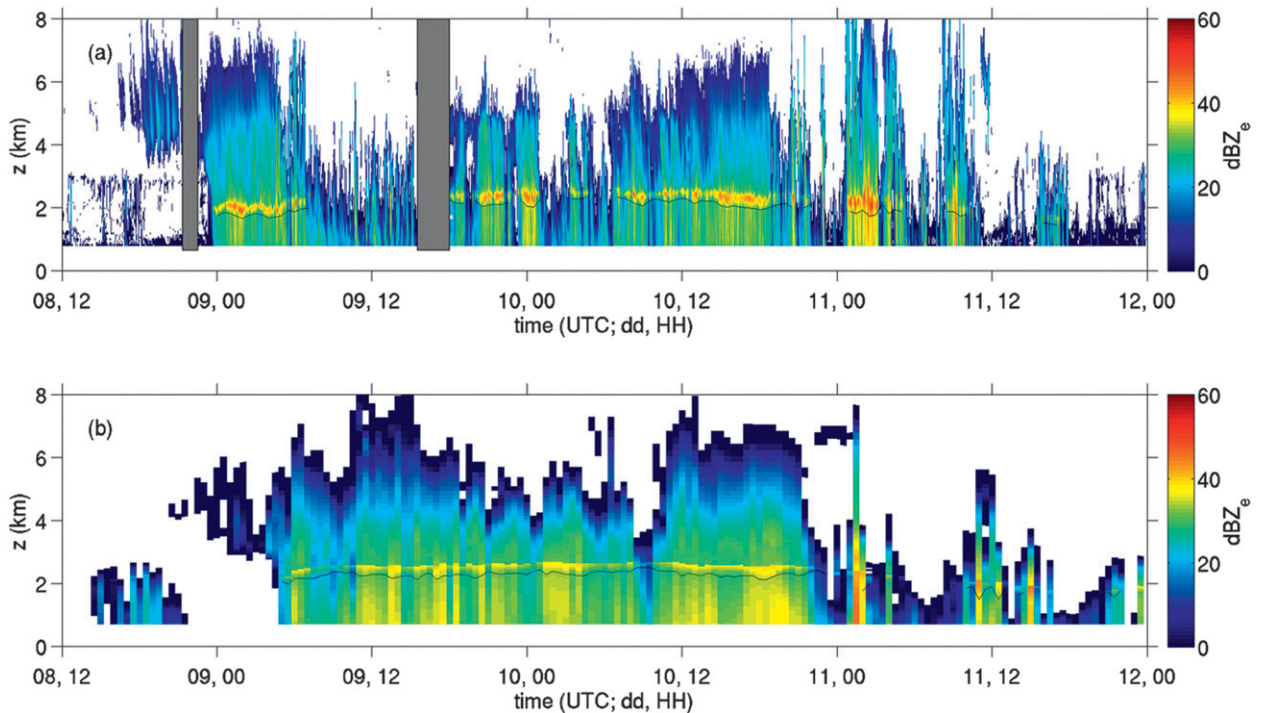
FIG. 7. S-band profiling radar time–height sections of Z_e at CFC from observations and WRF, shaded according to color bar. (a) Observed Z_e, plotted every 1 min. (b) WRF-simulated Z_e, plotted every 30 min and calculated as described in appendix B. Gray-shaded areas in (a) denote times when radar profiler was malfunctioning. The thin black line in (a) and (b) represents the objectively identified z_{BBmin}.

b. Model results

Synoptic-scale storm evolution in the WRF simulation is presented in Figs. 9 and 10. The simulation produces a similar progression of clouds, SLP, and IWV as found in Figs. 3 and 5, with a sequence of two cyclones bringing high clouds and very moist south-southwesterly flow to the study area. Using 30-min output from the innermost WRF domain, time series of 2-m temperature and accumulated precipitation from the nearest WRF grid point to the surface stations are shown in Figs. 4b,d. The simulation shows surface frontal signatures at the station locations, but the warm-frontal passage is more pronounced at SHS and less pronounced at the mountain stations than in the observations. The decrease in temperature with elevation is generally well captured, but temperatures do not reach 0°C during the storm at BBD as observed. WRF produces continuous precipitation throughout the event, with the largest rates occurring during the frontal passages, as observed. Also, as in the observations, there is a large orographic enhancement of rainfall across the station network. However, the modeled orographic enhancement is excessive, with substantially too much precipitation at the high sites and too little at SHS. The later underprediction is

mostly due to a lack of cold-frontal rainfall at SHS in WRF.

Vertical profiles of modeled wind, θ_e, and q_v at the grid point nearest to SHS are shown in Figs. 11a–d. The structure of the modeled frontal passages agrees well with observations, although the simulated warm-frontal passage is about 6 h later than observed (cf. Fig. 6). During the storm, strong directional sheer is found near 1 km MSL separating southwesterly flow aloft from along-barrier south-southeasterly flow near the surface. The simulation also reproduces the steadily elevated IWV throughout the duration of the storm as well as the variations in IWV associated with frontal passages (Fig. 11e). There is some evidence for thermodynamic modification by melting, as there is a modest local minimum in θ_e just below z_{0C} throughout much of the period between 1200 UTC 9 February and 0000 UTC 11 February.

Simulated Z_e profiles from the grid point nearest CFC (Fig. 7b) reproduce several of the major observed features, including virga echoes as the warm front approaches, a maximum in echo intensity during the cold-frontal passage, and a transition to convective echoes during and after the cold front. Although the magnitude of the peak BB intensity is not well captured by WRF,
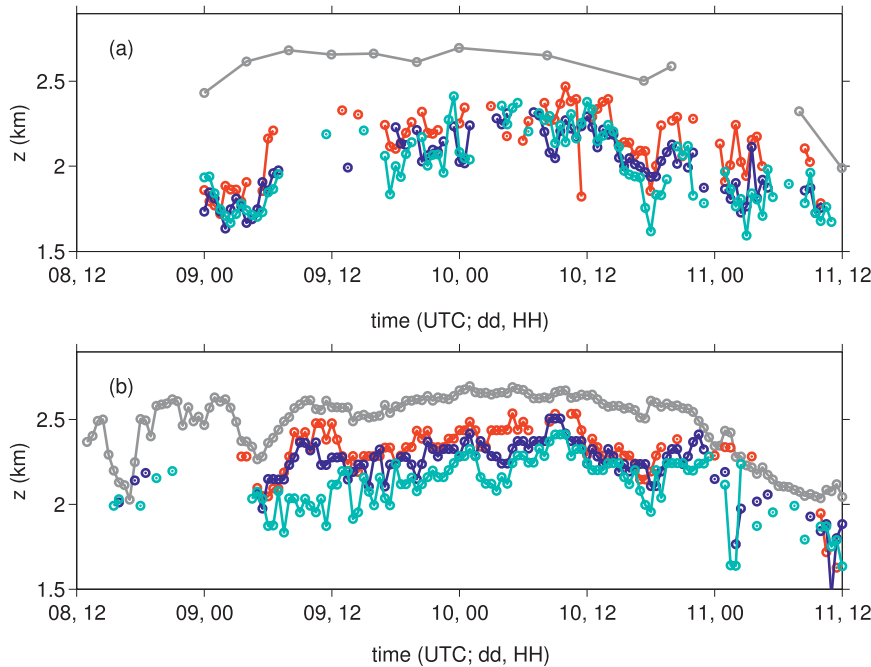
FIG. 8. Time series of z_{0C} at SHS (gray line, elevation 50 m MSL) and z_{BBmin} at SHS (red), CFC (blue, 636 m MSL), and ATA (cyan, 1085 m MSL) (a) from HMT balloon and radar profiler observations and (b) from 30-min WRF output.

the simulated depth and height of the BB layer is reasonable. A major deficiency in the simulation is an excessive depth and intensity of echoes from about 0800 to 1600 UTC 9 February, when observations show only shallow and light NBB rain. Excessive orographic precipitation during this period is the main deficiency of the simulation.

Model-derived estimates of z_{BBmin} and z_{0C} show a similar evolution to the observations (Fig. 8b). Both z_{BBmin} and z_{0C} rise and fall with the frontal passages, and are relatively steady in between. At SHS, z_{0C} is located at about 2.6 km MSL with z_{BBmin} about 200 m below, which is a similar melting distance as seen in the observations. The mountain sites consistently show z_{BBmin} lower than upwind at SHS. The values of Δz_{BBmin} are 69 m at CFC and 201 m at ATA (Table 3). These values are not directly comparable with observations owing to differences in the mesoscale storm structures, in particular the presence of shallow NBB rain in the observations that is absent from the simulation. However, the consistent lowering of the melting layer toward the terrain by around 150 m appears to be captured by WRF in a realistic way. This suggests WRF adequately represents the processes responsible for controlling snow line variations, making it useful as a diagnostic tool for understanding the responsible mechanisms. Such a diagnosis will be the subject of the next section.

5. Mechanisms

a. Mechanisms: Cross-sectional diagnostics

To diagnose the mechanisms responsible for lowering the snow line over the Sierras, we first analyze a specific time when there was a particularly large Δz_{BBmin} and heavy precipitation in the WRF simulation: 1100 UTC 9 February. This roughly corresponds to the end of the simulated warm-frontal passage (Fig. 11). This is not directly comparable to the same time in the observations, since the observed passage was several hours earlier (around 0600 UTC). However, large Δz_{BBmin} occurred during the observed frontal passage (Fig. 8a). The simulated 500-m winds and 1-h precipitation are plotted at 1100 UTC 9 February for the innermost WRF domain in Fig. 12. Near the coastline there are strong winds from the southwest to south-southwest, but nearer to the Sierras these are turned to south-southeast to southeast, as is typical of low-level blocked flow in the region (e.g., Parish 1982; Neiman et al. 2010). Maximum precipitation rates are found over the northern Sierra and exceed 10 mm h^{-1}.

Vertical cross sections from the WRF output, taken along the HMT transect and roughly parallel to the upwind incoming flow (thick line in Fig. 12), are shown in Fig. 13. Both z_{0C} and the bottom of the q_f field (and hence z_{Smin}) descend toward the terrain
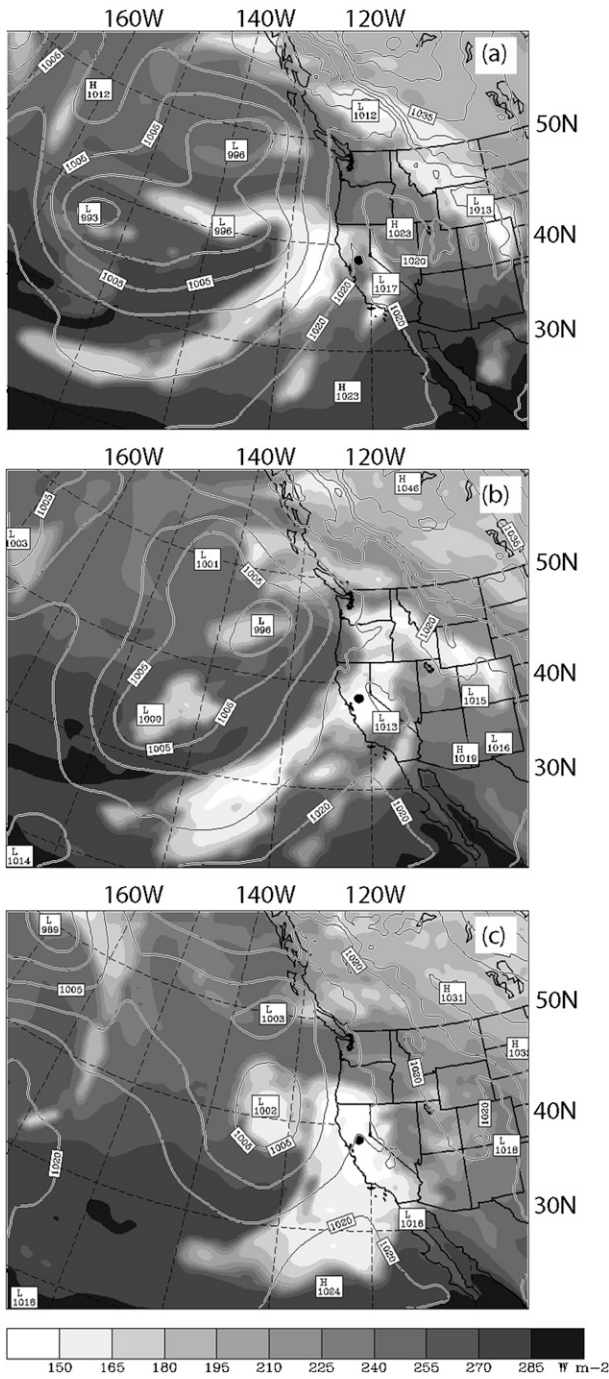
FIG. 9. Sequence of synoptic maps from the outermost WRF domain showing SLP (contoured every 5 hPa) and top-of-atmosphere outgoing longwave radiation (shaded according to scale). Times are (a) 1800 UTC 8 Feb, (b) 1200 UTC 9 Feb, and (c) 1200 UTC 10 Feb. Black dot shows the location of SHS.

(Fig. 13a). Downwind of the terrain z_{0C} rises sharply, associated with adiabatic warming of plunging down-slope winds. Comparing values at the foot of the terrain (distance = 180 m) to values at the mountainside, z_{0C}
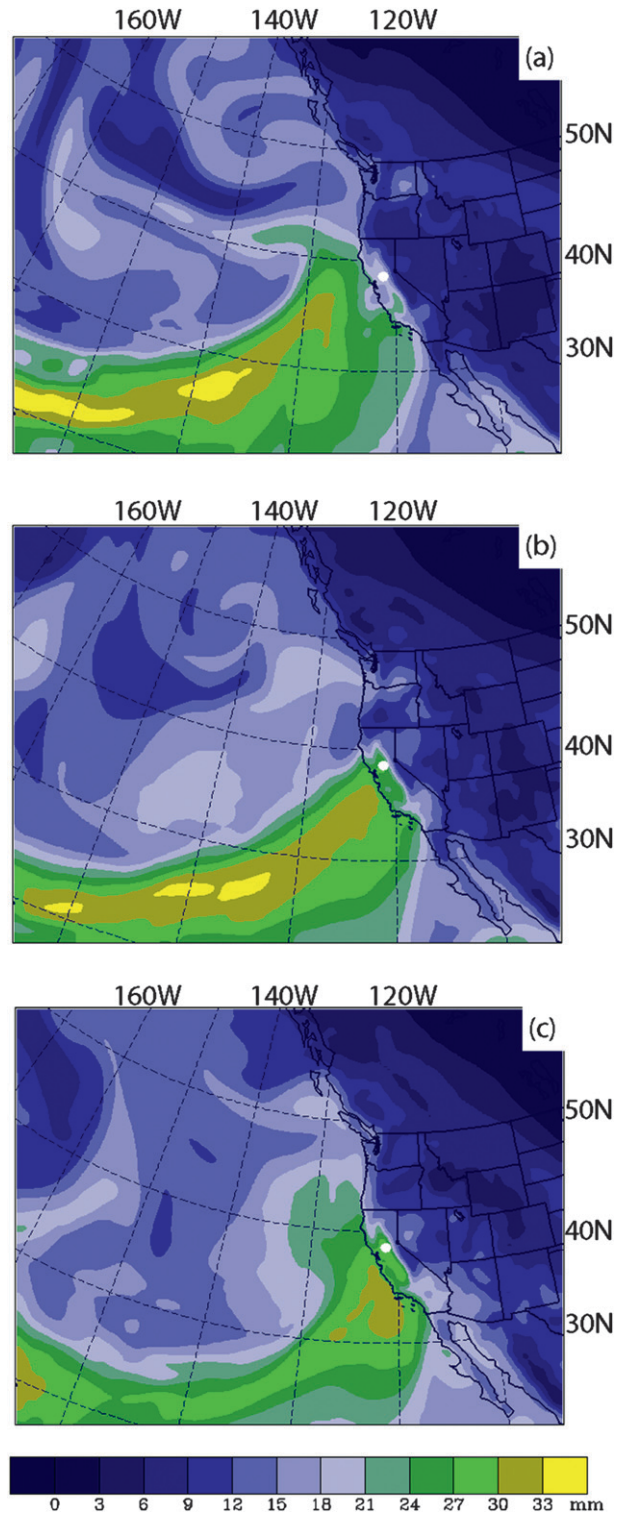

FIG. 10. Sequence of synoptic maps from the outermost WRF domain showing vertically integrated water vapor (shaded according to scale). Times are (a) 1800 UTC 8 Feb, (b) 1200 UTC 9 Feb, and (c) 1200 UTC 10 Feb. White dot shows the location of SHS.
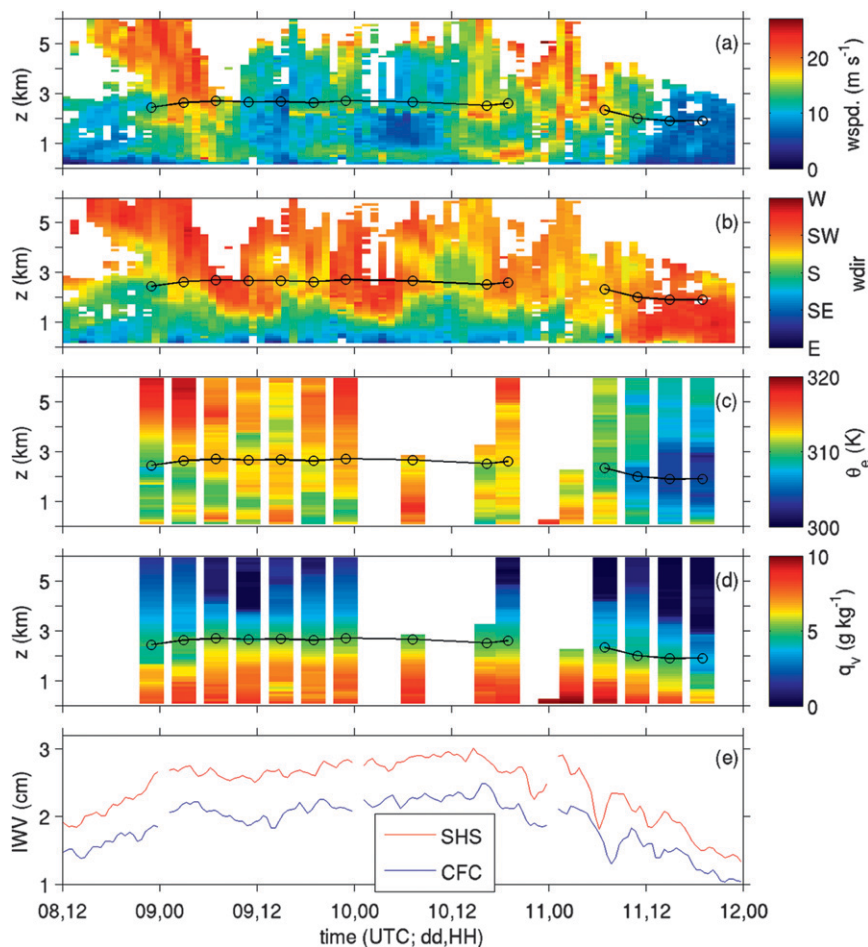
FIG. 11. Time–height sections from WRF simulation at SHS. Color shading shows (a) wind speed, (b) wind direction, (c) θ_e, and (d) q_v. The thin black line is z_{0C}. (e) IWV at SHS and CFC.

descends by about 500 m, and z_{Smin} descends by about 600 m.

At this time, the WRF-simulated profiler–based estimate from CFC or ATA give Δz_{BBmin} values of only 203 and 364 m—substantially smaller than the full z_{Smin} lowering. This discrepancy arises because much of the simulated lowering occurs just a few kilometers southwest of where z_{0C} and z_{BB} intersect the terrain (see Fig. 13a) and, as a result, is not captured by the profiler network because of the limited horizontal distribution of profiler sites.

The importance of D_{melt} variations in causing the lowering of z_{Smin} is quantified by measuring the increase in D_{melt} toward the terrain. This indicates about 100 m of snow line lowering due to D_{melt} variations, with the remainder attributable to variations in z_{0C}. Two classes of mechanisms may cause the lowering of z_{0C}. The first is pseudoadiabatic processes, wherein the rearrangement of air masses without any diabatic heat sources (other than latent heating from condensation)

produces horizontal variations in temperature and z_{0C}. This can arise because of orographic lifting of stratified air (e.g., Marwitz 1987; Minder et al. 2011) or because of horizontal transport of air masses with different properties. The second is diabatic processes, wherein cooling associated with latent heat absorption during melting, radiation, or turbulent fluxes may act to cool the air locally over the windward slopes.

To examine the role of pseudoadiabatic processes, we first consider the thermodynamic structure of the flow with a cross section of θ_e (Fig. 13b). Upwind of the Sierras, θ_e shows significant stratification, increasing with height up to about 1.5 km. This stratification is a necessary condition for pseudoadiabatic cooling by orographic lifting to cause a lowering of z_{0C} (Minder et al. 2011). However, examining the cross- and along-mountain components of the wind reveals that the flow kinematics are more complex than simple 2D orographic lifting. There is a cross-mountain low-level jet of 16–18 m s^{-1} that lifts toward the terrain, and joins a

TABLE 3. Event-averaged snow line statistics at CFC and ATA. Top row is from observations; all others are for WRF simulations. CNTL is control simulation. NO_MC is simulation without melting-induced cooling. DX_ and DZ_ are for model-resolution experiments. MP_ is for microphysics sensitivity experiments. The left section of the table is for radar-based estimates of the snow line. The right section is for mixing-ratio-based estimates. In the left section the value of Δz_{0C} is averaged over all times with a BB detected at both SHS and the station of interest. In the right section the value of Δz_{0C} is averaged over all times that z_{Smin} is defined at both SHS and the station of interest. Units are meters.

Run name	Δz_{BBmin}		Δz_{0C}		$(\Delta D_{melt})_{BBmin}$		Δz_{Smin}		Δz_{0C}		$(\Delta D_{melt})_{Smin}$	
	CFC	ATA	CFC	ATA	CFC	ATA	CFC	ATA	CFC	ATA	CFC	ATA
Obs	−123	−150										
CNTL	−69	−201	−17	−52	52	148	−109	−213	−16	−48	93	165
NO_MC	−64	−150	4	−7	67	132	−102	−183	1	−12	103	171
DX_3	−101	−140	−21	−48	79	92	−138	−172	−20	−43	119	128
DX_9	−124	−165	−60	−83	64	82	−139	−194	−57	−76	83	116
DX_27	−107	−156	−49	−62	58	94	−98	−180	−43	−68	55	116
DX_3_DZ_80	−93	−131	−26	−54	67	78	−127	−158	−24	−51	103	108
MP_PLIN							−67	−57	−34	−58	33	−1
MP_GDRD							−100	−124	−29	−49	70	75
MP_THMP							−150	−181	−44	−69	106	112
MP_WDM6							−138	−197	−10	−30	128	167
MP_MOR2							−29	−42	−48	−63	−50	−92
MP_MY2							−101	−121	−46	−66	55	54

deeper layer of strong cross-mountain wind near the crest (Fig. 13c). Below this flow, largely in the low-θ_e air mass, is a layer of weak cross-mountain winds and strong along-mountain winds. Over the windward slopes of the Sierras this takes the familiar form of a SBJ, with along-mountain flow exceeding 12 m s^{-1} (Fig. 13d). The low-θ_e air in this along-barrier flow is largely composed of cool and dry prefrontal air that has been blocked by the terrain. Since much of the lowering of z_{0C} occurs in a transition region between strong along-barrier and cross-barrier flow, the relative importance of pseudoadiabatic cooling due to lifting and along-barrier transport of low-θ_e air is not immediately clear.

Further insight into the role of pseudoadiabatic processes is provided by air parcel back-trajectory analysis. Figure 14 shows eighteen 3-h back trajectories of air parcels (calculated using 2-min WRF output) that end at z_{0C} on the transect at the time of the cross sections in Fig. 13. Most of the parcels rise by between 50 and 150 m as they approach z_{0C} (Fig. 14b). Parcels 1–13 follow the cross-mountain flow along the section as they approach z_{0C} just upwind of the terrain (Fig. 14a). In contrast, parcels 14–18 participate, to varying degrees, in the along-barrier flow before reaching z_{0C} over the windward slopes.

A simple parcel model can be used to examine the role of pseudoadiabatic processes in determining the structure of z_{0C} (Minder et al. 2011). For each trajectory the WRF-simulated temperature, humidity, elevation, and pressure at the initial time are used as input into an external thermodynamic parcel-model calculation. A parcel's temperature is calculated as it is lifted, first dry adiabatically to saturation and then moist pseudoadiabatically.

For each parcel, the model predicts the height it reaches z_{0C} in the absence of diabatic processes other than condensation. The results for each trajectory are plotted in Fig. 15a, which shows the parcel-model-predicted z_{0C} scattered against the actual WRF trajectory z_{0C}. While for individual trajectories the parcel model has mixed success predicting z_{0C}, it succeeds in predicting the
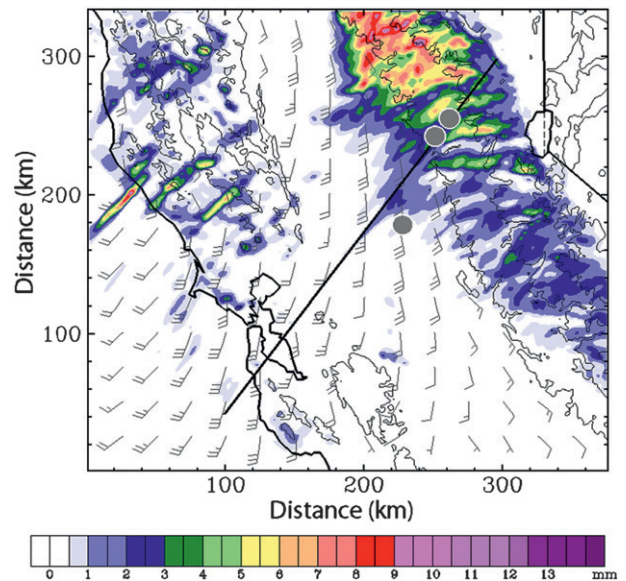

FIG. 12. Winds at 500 m MSL [full barb every 10 knots (1 knot = 0.51 m s^{-1}) and precipitation from the previous hour (color shading) at 1100 UTC 9 Feb. Axis tick marks are shown every 20 km. The thick black line shows the location of the sections shown in Fig. 13. Gray dots show the locations of the profiling radars at SHS, CFC, and ATA.
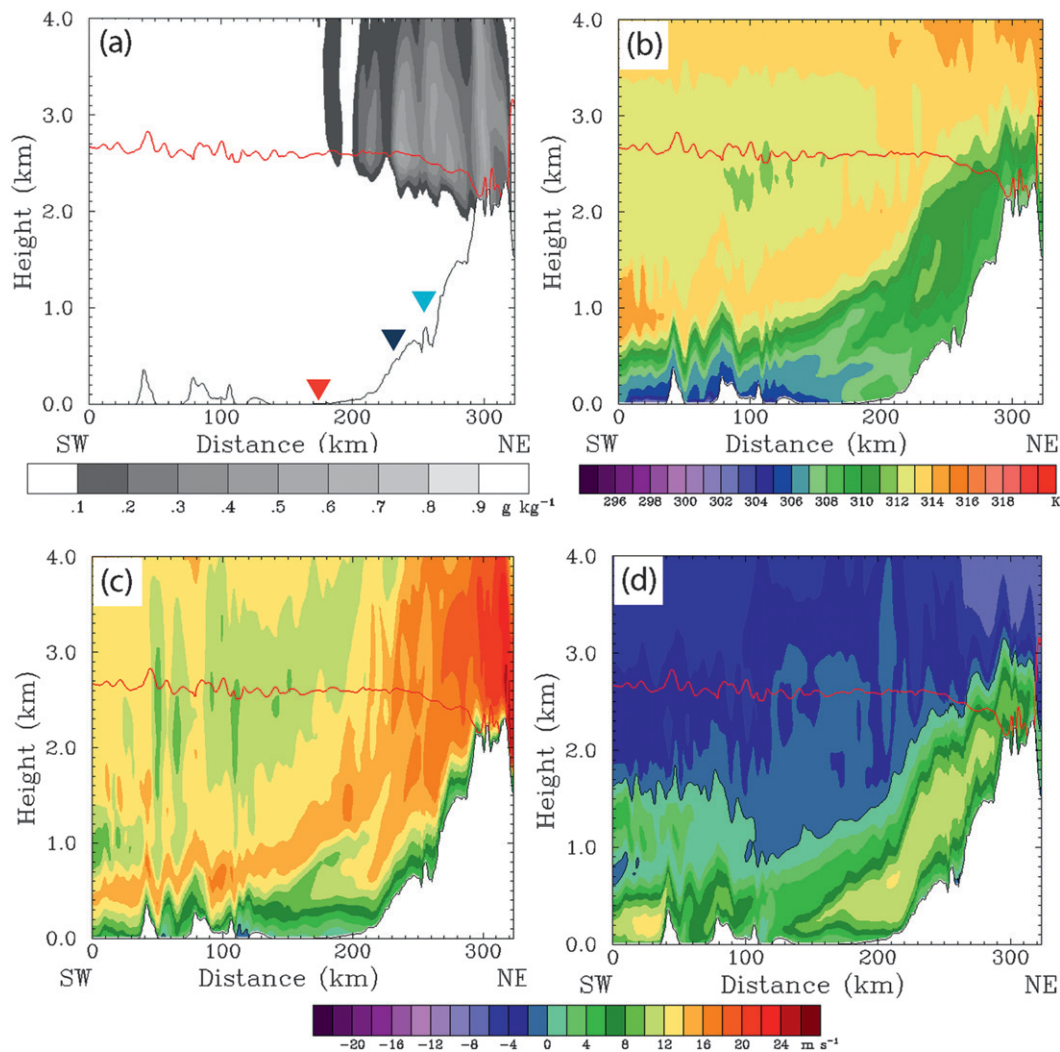
FIG. 13. Cross section through WRF output at 1100 UTC 9 Feb, along HMT network (black line in Fig. 12). The red line is z_{0C}. Shading shows (a) total mixing ratio of snow and graupel, (b) θ_e, (c) cross-mountain wind speed (positive is from left to right), and (d) along-mountain wind speed (positive is into the section, black line at zero). In (a), triangles show the approximate locations and elevations of the profiling radars at SHS (red), CFC (blue), and ATA (cyan).

significantly lower z_{0C} found in the along-barrier group of trajectories.

The error in the parcel-model prediction of z_{0C} is scattered against the WRF-predicted change in θ_e along each trajectory in Fig. 15b. Since θ_e is conserved for moist pseudoadiabatic processes (i.e., in the absence of diabatic sources and sinks other that local condensation and evaporation), these two variables show a strong anticorrelation: larger parcel-model overpredictions of z_{0C} correspond to large amounts of cooling in θ_e. This is particularly true for trajectory 18—the trajectory ending nearest to the mountainside and experiencing the most cooling in θ_e. Taken together, the panels of Fig. 15 suggest that along the transect there is about a 250-m lowering of z_{0C} that is due to pseudoadiabatic processes

(largely associated with differences in the cross-barrier and blocked along-barrier airstreams) that can be captured with a simple parcel model. Yet, there is an additional approximately 200 m of z_{0C} lowering due to diabatic cooling that is unaccounted for by the parcel model.

To identify the source of this diabatic cooling, θ_e budgets are considered along each of the trajectories. For each trajectory WRF output is used to calculate θ_e every 2 min, as well as the instantaneous θ_e tendencies due to parameterizations of radiation, boundary layer turbulence, and microphysics. The microphysical tendency is further separated into contributions from various processes. For three representative trajectories, Fig. 16 shows changes in θ_e (relative to the value at 1020 UTC 9 February) for the 2 h before the parcels reach z_{0C}.
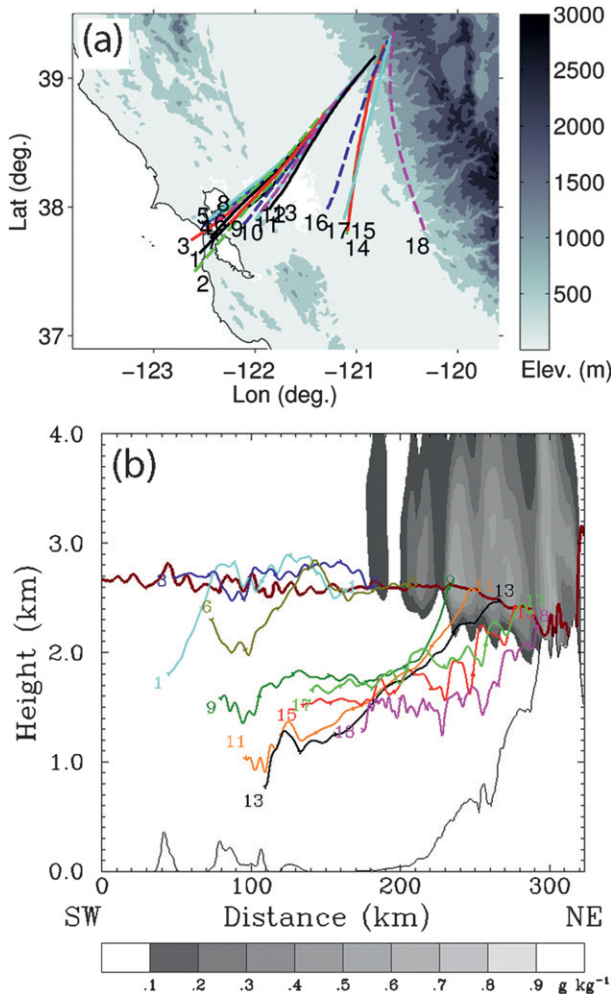
FIG. 14. Three-hour back trajectories ending at z_{0C} along the section at 1100 UTC 9 Feb. (a) Horizontal map including trajectory ID numbers and gray-shaded terrain elevation. (b) Total mixing ratio of snow and graupel (shading), z_{0C} (thick dark-red line), and selected back trajectories (thin lines).

Trajectories 5 and 10 come from the cross-barrier airstream and show little change in θ_e. In contrast, trajectory 18 flows along the barrier and experiences more than a 1.5-K decrease in θ_e, mostly in the hour before it reaches z_{0C}. The source of this cooling becomes clear when the integrated θ_e tendency due to absorption of latent heat by melting is plotted (dashed gray line). Almost all the reduction of θ_e found along both trajectories 10 and 18 can be accounted for by melting. Tendencies due to radiation, turbulent fluxes, and other microphysical phase changes make much smaller contributions (not shown). Thus, it appears that, at the time of the cross section, melting-induced cooling accounts for the approximately 200 m of z_{0C} lowering that is not accounted for by pseudoadiabatic processes.

b. Mechanisms: Storm-averaged diagnostics

The previous diagnostics quantified the mechanisms responsible for the snow line lowering on the mountainside at a given time. Next we consider the importance of the same mechanisms in explaining the event-averaged behavior of the snow line by using WRF-simulated profiles at SHS, CFC, and ATA to quantify the mechanisms that lower z_{BBmin} between the upwind and mountain profiler sites. The contribution due to melting-distance variations is given by $(\Delta D_{melt})_{BBmin}$, which is calculated as the event-averaged difference between $(D_{melt})_{BBmin}$ at SHS and each mountain site, such that $(\Delta D_{melt})_{BBmin} > 0$ corresponds to larger melting distances near the terrain. The contribution due to processes that lower z_{0C} is given as Δz_{0C}, the event-averaged difference in z_{0C} between SHS and each mountain site, considering only times when a BB was present.

The values of these metrics for CFC and ATA are given in Table 3. The difference between Δz_{0C} and $(\Delta D_{melt})_{BBmin}$ gives the total snow line lowering represented by Δz_{BBmin}. Based on this analysis, D_{melt} variations are responsible for about 75% of the lowering of z_{BB} at the two mountain profiler sites, while the remaining 25% is caused by z_{0C} lowering.

To diagnose the relative contributions of pseudoadiabatic processes and melting-induced cooling an additional simulation is conducted. In this simulation atmospheric cooling due to melting of snow and graupel is eliminated from the model's thermodynamic equation. This suppression is imposed from 0600 UTC 9 February—just after the beginning of precipitation—until the end of the simulation. The results of this simulation (NO_MC) are shown in Table 3. Without cooling from melting, Δz_{0C} at the profiler sites is essentially eliminated, suggesting that cooling from melting is the primary cause of the storm-averaged cooling at these sites. At CFC Δz_{BBmin} is barely affected (primarily because Δz_{0C} was small in the control simulations), but it is reduced by about 25% at ATA.

These results contrast with those of section 4a by indicating a larger role for D_{melt} variations and a smaller role for z_{0C} variations. This is due in part to the focus on profiler sites in this section, which fails to capture the lowering of z_{0C} and z_{BBmin} that occurs very close to where z_{0C} and z_{BBmin} intersect the terrain (e.g., Fig. 13). At 1100 UTC 9 February (the cross-sectional analysis time), ΔD_{melt} accounts for all the z_{BBmin} lowering at CFC and about 75% at ATA, which is consistent with the event-averaged statistics. Thus it appears that D_{melt} variations are the primary cause of the profiler-observed z_{BBmin} lowering, but very near to the mountain (at ATA and beyond) pseudoadiabatic and melting-induced cooling cause substantial additional lowering.
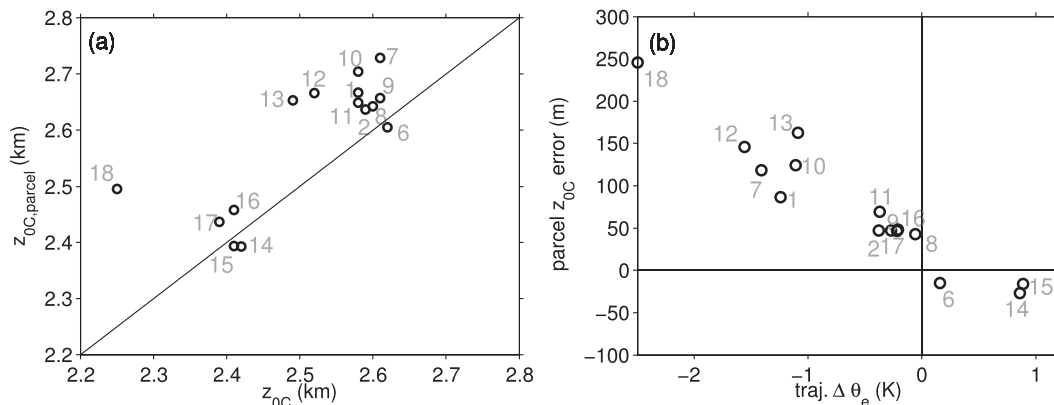
FIG. 15. Diagnostics from WRF trajectories and parcel model. (a) Parcel-model-predicted z_{0C} scattered against actual WRF trajectory z_{0C} for each trajectory in Fig. 13. (b) Difference between parcel-model z_{0C} and WRF trajectory z_{0C} scattered against change in θ_e along each WRF trajectory.

6. Sensitivity experiments

a. Spatial resolution

The sensitivity of WRF results to horizontal resolution is explored with three additional runs, using horizontal grid spacing of 3, 9, and 27 km. This is accomplished using an identical model domain as in the control experiment, but removing one, two, or all three of the inner nests. Results of these simulations in Table 3 (DX_3, DX_9, and DX_27) show that the lowering of z_{BBmin} is present at both mountain sites in all of the coarser simulations. These runs all show a more gradual lowering of z_{BBmin}, with less lowering at ATA and more at CFC relative to CNTL. However, there is no monotonic tendency toward larger or smaller values of Δz_{BBmin} with decreasing resolution. The partitioning of mechanisms changes somewhat at coarser resolution, with Δz_{0C} playing a more important role relative to CNTL.

The sensitivity to vertical resolution is explored by resimulating the DX_3 case with vertical grid spacing in the lowest 3 km increased to 80–110 m (compared to 40–60 m in CNTL). This simulation, DX_3_DZ_80, gives very similar results to the DX_3 case in terms of the magnitude of Δz_{BBmin} and the partitioning between Δz_{0C} and ΔD_{melt}. This is surprising, since the vertical grid spacing in this case is very close to the mean value of Δz_{BBmin}, and thus the lowering should be barely resolved.

b. Microphysical parameterization

The sensitivity of WRF results to microphysical parameterizations is also explored by resimulating the case using six of the other schemes available in WRF, version 3.2.1. The prognostic variables, melting parameterization, and source material for these schemes are summarized in Table 4. They are all bulk schemes

that represent the size distribution of microphysical species with either one prognostic variable (the mixing ratio q) or two prognostic variables (q and the number concentration N). Melting is parameterized generally following either Rutledge and Hobbs (1983) or Wisner et al. (1972). The former neglects humidity effects on melting rates, while the latter attempts to capture them.
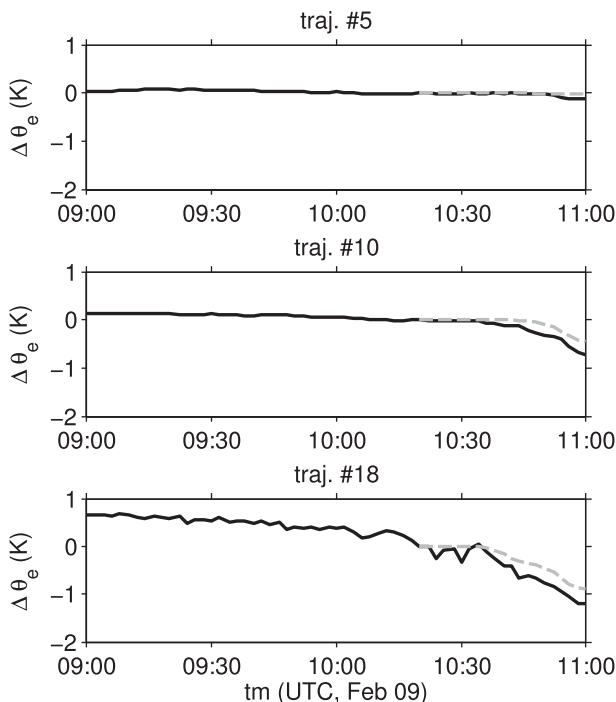

FIG. 16. Accumulated change in θ_e from 0900 to 1100 UTC 9 Feb for three selected WRF trajectories (black lines), defined such that $\Delta \theta_e = 0$ K at 1020 UTC. Also plotted is the accumulated θ_e tendency due to latent heat absorbed by melting from 1020 to 1100 UTC (dashed gray lines).

TABLE 4. Summary of microphysical schemes used in section 6b. Scheme name is given in first column. The prognostic variables are given in the second column: q is mixing ratio, N is number concentration, and subscripts v, c, i, r, s, g, h, and ccn are for water vapor, cloud liquid water, cloud ice, rain, snow, graupel, hail, and potential cloud condensation nuclei. Type of melting parameterization used is given in the third column: RH83 follows Rutledge and Hobbs (1983) and W72 follows Wisner et al. (1972). Papers describing the schemes are cited in the fourth column.

Scheme (abbreviation)	Prognostic variables	Melting	Citation
WSM6	$q_v, q_c, q_i, q_r, q_s, q_g$	RH83	Hong et al. (2004); Hong and Lim (2006)
Purdue–Lin (PLIN)	$q_v, q_c, q_i, q_r, q_s, q_g$	W72	Lin et al. (1983)
Goddard (GDRD)	$q_v, q_c, q_i, q_r, q_s, q_g$	RH83	Tao et al. (2003)
Thompson (THMP)	$q_v, q_c, q_i, q_r, q_s, q_g, N_r$	RH83	Thompson et al. (2004, 2008)
WDM6	$q_v, q_c, q_i, q_r, q_s, q_g, N_{ccn}, N_c, N_r$	RH83	Lim and Hong (2010)
Morrison two-moment (MOR2)	$q_v, q_c, q_i, q_r, q_s, q_g, N_i, N_r, N_s, N_g$	RH83	Morrison et al. (2009)
Milbrant–Yau two-moment (MY2)	$q_v, q_c, q_i, q_r, q_s, q_g, q_h, N_c, N_i, N_r, N_s, N_g, N_h$	W72	Milbrandt and Yau (2005a,b)

Detailed discussions of the differences between schemes are found in Skamarock et al. (2008), Lin and Colle (2009), and Jankov et al. (2009). To save computational expense, and in light of the similar results from the DX_3KM runs, these sensitivity experiments were conducted using 3-km horizontal grid spacing. To avoid deriving simulated reflectivity fields consistent with each of these schemes, hydrometeor mixing ratios are used directly to calculate $z_{S\min}$. For the experiments with WSM6, Table 3 shows that $z_{S\min}$ gives broadly similar results to $z_{BB\min}$.

Figure 17 shows cross sections of z_{0C} and q_f for each of these runs at 1100 UTC 9 February. All the simulations show a lowering of z_{0C} and the bottom of the q_f field toward the terrain. The lowering of z_{0C} is similar in all seven simulations, with z_{0C} intersecting the terrain near the highest mountain peak in the section. The q_f field varies substantially between schemes, both in terms of its horizontal extent and its peak magnitude. Still, at this time, the lowering of the bottom of the q_f field toward the terrain is fairly similar for most schemes, intersecting the terrain between 2 and 2.1 km MSL. The exception is the MP_MOR2 simulation, which melts snow and graupel immediately below z_{0C}, giving a significantly higher mountainside rain–snow boundary. The very small D_{melt} in MP_MOR2 is almost certainly unrealistic, based, for instance, on the depth of the observed BB in Fig. 8.

All schemes produce an event-averaged lowering of $z_{S\min}$ between the profiler locations (Table 3); however, the magnitude varies substantially, with $\Delta z_{S\min}$ at ATA ranging from -42 (MP_MOR2) to -197 m (MP_WDM6). The simulations are in general agreement with regards to the lowering of z_{0C}, producing a Δz_{0C} at ATA of between -50 and -70 m. The larger source of spread in $\Delta z_{S\min}$ stems from the differences in D_{melt} variations between the simulations. At ATA, ΔD_{melt} varies between 167 (MP_WDM6) and -92 m (MP_MOR2). Because of the many differences between

schemes it is difficult to assess the source of these variations. However, schemes that do not account for humidity effects on melting rates have larger ΔD_{melt} than those that do (with the exception of MP_MOR2, which exhibits unrealistic D_{melt} values), suggesting that details of melting parameterization may play a role. The broad agreement in terms of Δz_{0C} and the large discrepancy in ΔD_{melt} mirrors the results found by Minder et al. (2011) for semi-idealized 2D simulations.

7. Discussion and conclusions

Through analysis of 3 yr of profiling radar observations this study has shown that a mesoscale lowering of the snow line over the windward slopes of the northern Sierra Nevada is a robust and likely climatological feature. The typical observed lowering of about 170 m is large enough to have important implications for snow accumulation and runoff. Thus, efforts should be made to account for these effects in forecasts and projections of regional hydrometeorology, either through real-time radar observations (e.g., White et al. 2002; Maurer and Mass 2006) or through high-resolution numerical modeling (e.g., Tobin et al. 2012; Thériault et al. 2012).

High-resolution simulations of Sierra Nevada snow lines with a mesoscale numerical model (WRF) were compared with detailed mesoscale observations for a prototypical storm. In general, the spatial and temporal variations of the snow line are captured by WRF, despite some biases in the model's simulation of precipitation intensity and timing of frontal passages. This is encouraging, in that it suggests that such models can be useful for forecasting and understanding mesoscale snow line behavior. Although high-resolution simulations are desirable for resolving the snow line's behavior on the mesoscale, results do not appear to be strongly sensitive to model grid spacing. In contrast, the choice of microphysical parameterization has important impacts on the
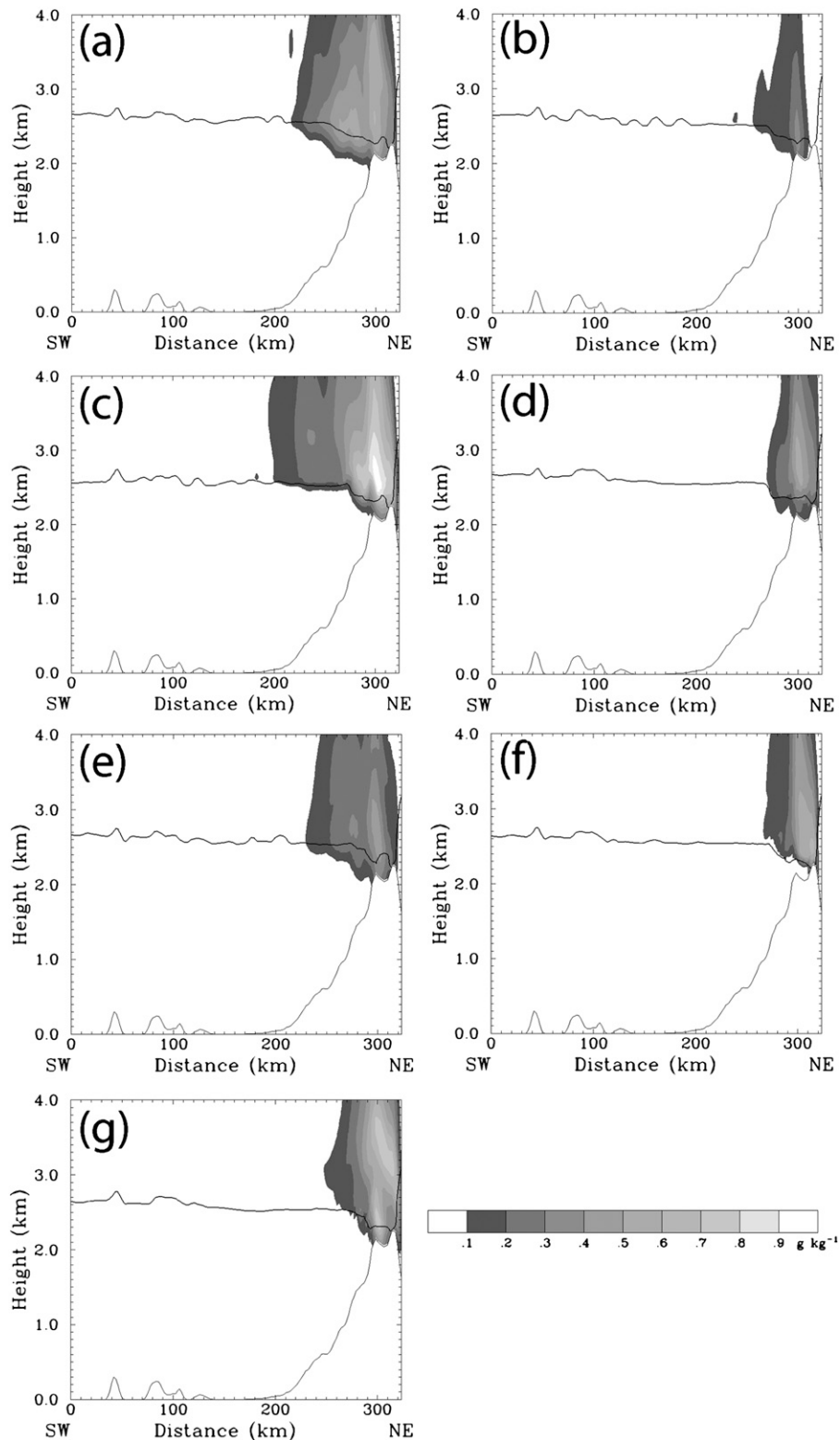
FIG. 17. WRF cross section for runs using different microphysical parameterizations and a 3-km horizontal grid (see Tables 1–2). All sections are along the line in Fig. 12 at 1100 UTC 9 Feb, and show z_{0C} (thick black line) and the frozen-hydrometeor mixing ratios (as in Fig. 13a). The panels correspond to the following runs: (a) DX_3KM, (b) MP_PLIN, (c) MP_GDRD, (d) MP_THMP, (e) MP_WDM6, (f) MP_MOR2, and (g) MP_MY2.

melting distance of frozen hydrometeors that in turn influence the snow line. Model results indicate that a large fraction of the snow line lowering occurs over short horizontal distances and very near to the mountainside. As a result radar profiler–based estimates from typical networks with only a handful of profilers will generally underestimate the lowering.

Results of WRF simulations were also used to diagnose the physical mechanisms responsible for the mesoscale descent of the snow line. Over the mountainside, increases in frozen-hydrometeor melting distance, enhanced melting-induced cooling, and along-barrier pseudoadiabatic transport of low-θ_e air all play an important role in lowering the snow line. All three of these mechanisms are quantitatively important for the case examined. This is in general agreement with the semi-idealized modeling results of Minder et al. (2011). However, their 2D simulations were unable to capture the role played by along-barrier flow of terrain-blocked prefrontal air.

For the case studied here, it is likely that the strong winds found at the height of the melting layer played an important role in limiting the residence time of air parcels in the melting region, and hence the importance of melting-induced cooling (Unterstrasser and Zängl 2006; Minder et al. 2011). In colder storms (with low snow lines), or when the incoming flow is strongly terrain blocked or constrained in valleys, melting-induced cooling may play a more central role (e.g., Thériault et al. 2012). Such scenarios may help to explain the kilometer-scale snow line drops observed by Marwitz (1983, 1987).

Since this study has focused largely on a single storm and a specific region, future work will examine other regions and synoptic conditions to investigate storm-to-storm and geographic variability of the snow line's mesoscale behavior. A better understanding of the mesoscale response of the snow line to large-scale forcing should also help refine our understanding of the response of mountain snow to climate change and variability.

APPENDIX A

Objective Brightband Height Analysis

In the present study we objectively identify the elevation of the BB peak z_{BB} and the BB bottom z_{BBmin} from both S-band and 915-MHz profiling Doppler radar data. For practical reasons we use two similar but distinct methods for identifying these two variables.

Calculation of z_{BB} values used in multiyear statistics (section 3) employs the operational methods described in White et al. (2002). This method uses profiles of V_r and SNR, with range resolutions of 106 m at SHS and 60 m at CFC and ATA. Profiles with low-level (below 3 km MSL) V_r less than -2.5 m s^{-1} and SNR greater than 52 dB are selected as candidates for BB identification. The lower portion of the BB is identified by searching for a 2.5 dB or greater increase in SNR and 1.5 m s^{-1} or greater decrease in V_r over three range gates moving upward [following White et al. (2002)]. For SHS (106-m gate spacing) this corresponds to SNR and V_r thresholds of 12 dB km^{-1} and -7 m s^{-1} km^{-1}, respectively. With the finer vertical resolution of the ATA and CFC profilers (60-m gate spacing), the SNR and V_r thresholds are 21 dB km^{-1} and -13 m s^{-1} km^{-1}, respectively.

When a BB is identified, z_{BB} is calculated as the elevation of the peak SNR in the 525-m layer above the threshold gradients. For each hour, a median value of z_{BB} is calculated. For the 915-MHz profiler at SHS, both vertical and off-vertical beams are used. To eliminate false detections, all z_{BB} values that differ from the hourly median by more than two range gates are discarded. For hours with at least six remaining profiles, hourly averaged z_{BB} is calculated, which is used in the analysis of section 3.

For the case study of section 4 we focus on the bottom of the BB, z_{BBmin}, to give a better measure of the lower limit of snowfall and to facilitate comparison with WRF (which places z_{BB} too close to the top of the BB). Detection of z_{BBmin} follows the same framework as above, but with some important distinctions. For the SHS profiler, only 60-m-range-resolution data from vertical beams is used, giving comparable vertical resolution to that at the S-band profiler sites. Vertical gradients are still used to identify the lower portion of the BB, but they are calculated across pairs of range gates (instead of three gates), and lower threshold values are used (5 dB km^{-1} for SNR and -5 m s^{-1} km^{-1} for V_r) to

identify the BB bottom with more sensitivity. When these threshold gradients are exceeded, the lower of the two gates used in the difference is identified as z_{BBmin}. Next, 30-min median values of z_{BBmin} are computed for all 30-min windows with at least six BB detections. Outliers differing from the median by more than 200 m are discarded. Additional outliers are discarded if they differ from the event-mean value by more than three standard deviations. After eliminating outliers, 30-min average z_{BBmin} is calculated.

APPENDIX B

Model-Simulated Z_e and V_r

Assuming Rayleigh scattering, Z_e is computed as

$$(Z_e)_r = \int_0^\infty N(D)D^6 \, dD, \tag{B1}$$

where D is raindrop diameter, and $N(D)$ is the hydrometeor size distribution expressed in number of particles per unit diameter range. For snow and graupel Z_e is computed as

$$(Z_e)_{s,g} = \left(\frac{\rho_{s,g}}{\rho_i}\frac{|K_i|}{|K_l|}\right)^2 \int_0^\infty N(D)D^6 \, dD, \tag{B2}$$

where $|K_i|/|K_l| = 0.189$ is the ratio of dielectric constants for ice and liquid water, and $\rho_{s,g}/\rho_i$ is the ratio of the densities of modeled snow (100 kg m^{-3}) or graupel (500 kg m^{-3}) to that of solid ice (917 kg m^{-3}), which is used to convert from frozen hydrometeor diameter to equivalent diameter of a solid ice sphere. The above integrals are evaluated from predicted hydrometeor mixing ratios using the size distribution assumed by WSM6 [following, e.g., Fovell and Ogura (1988), and http://www.atmos.washington.edu/~stoeling/RIP_sim_ref.pdf]. Where snow and graupel are found at above-freezing temperatures, the increase in dielectric factor associated with melting and liquid water coating is represented by setting $|K_i|/|K_l| = 1$. While this treatment of the BB is admittedly simplistic [compared to, e.g., Fabry and Szyrmer (1999)], we deem it sufficient since we are primarily concerned with height and depth of the radar BB signature, which are relatively insensitive to assumptions about dielectric properties as compared to BB intensity (Fabry and Szyrmer 1999). The total Z_e is represented as a linear sum of the contributions from rain, snow, and graupel. We calculate V_r as a Z_e-weighted average of hydrometeor vertical motions using the fall speed–diameter relationships assumed in WSM6 and vertical air velocities predicted by WRF.

REFERENCES

Abatzoglou, J. T., 2011: Influence of the PNA on declining mountain snowpack in the Western United States. *Int. J. Climatol.,* **31,** 1135–1142, doi:10.1002/joc.2137.

Caldwell, P., 2010: California wintertime precipitation bias in regional and global climate models. *J. Appl. Meteor. Climatol.,* **49,** 2147–2158.

Carter, D. A., K. S. Gage, W. L. Ecklund, W. M. Angevine, P. E. Johnston, A. C. Riddle, J. Wilson, and C. R. Williams, 1995: Developments in UHF lower tropospheric wind profiling at NOAA's Aeronomy Laboratory. *Radio Sci.,* **30,** 977–1001, doi:10.1029/95RS00649.

Chen, F., and J. Dudhia, 2001: Coupling an advanced land surface–hydrology model with the Penn State–NCAR MM5 modeling system. Part I: Model implementation and sensitivity. *Mon. Wea. Rev.,* **129,** 569–585.

Das, T., M. D. Dettinger, D. R. Cayan, and H. G. Hidalgo, 2011: Potential increase in floods in California's Sierra Nevada under future climate projections. *Climatic Change,* **109** (Suppl.), 71–94, doi:10.1007/s10584-011-0298-z.

Duan, J., and Coauthors, 1996: GPS meteorology: Direct estimation of the absolute value of precipitable water. *J. Appl. Meteor.,* **35,** 830–838.

Dudhia, J., 1989: Numerical study of convection observed during the Winter Monsoon Experiment using a mesoscale two-dimensional model. *J. Atmos. Sci.,* **46,** 3077–3107.

Fabry, F., and T. Zawadzki, 1995: Long-term radar observations of the melting layer of precipitation and their interpretation. *J. Atmos. Sci.,* **52,** 838–851.

——, and W. Szyrmer, 1999: Modeling of the melting layer. Part II: Electromagnetic. *J. Atmos. Sci.,* **56,** 3593–3600.

Findeisen, W., 1940: The formation of the 0°C isothermal layer in fractocumulus and nimbostratus. *Meteor. Z.,* **57,** 49–54.

Fovell, R. G., and Y. Ogura, 1988: Numerical simulation of a midlatitude squall line in two dimensions. *J. Atmos. Sci.,* **45,** 3846–3879.

Guan, B., N. P. Molotch, D. E. Waliser, E. J. Fetzer, and P. J. Neiman, 2010: Extreme snowfall events linked to atmospheric rivers and surface air temperature via satellite measurements. *Geophys. Res. Lett.,* **37,** L20401, doi:10.1029/2010GL044696.

Hong, S.-Y., and J.-O. J. Lim, 2006: The WRF Single-Moment 6-class microphysics scheme (WSM6). *J. Korean Meteor. Soc.,* **42,** 129–151.

——, J. Dudhia, and S.-H. Chen, 2004: A revised approach to ice microphysical processes for the bulk parameterization of clouds and precipitation. *Mon. Wea. Rev.,* **132,** 103–120.

Houze, R., 1993: *Cloud Dynamics.* Academic Press, 573 pp.

Janjic, Z., 1996: The surface layer in the NCEP Eta Model. *Proc. 11th Conf. on Numerical Weather Prediction,* Norfolk, VA, Amer. Meteor. Soc., P2.1.

——, 2002: Nonsingular implementation of the Mellor-Yamada Level 2.5 scheme in the NCEP Meso model. NCEP Office Note 437, 61 pp.

Jankov, I., J.-W. Bao, P. J. Neiman, P. J. Schultz, H. Yuan, and A. B. White, 2009: Evaluation and comparison of microphysical algorithms in ARW-WRF model simulations of atmospheric river events affecting the California coast. *J. Hydrometeor.,* **10,** 847–870.

Kain, J. S., 2004: The Kain–Fritsch convective parameterization: An update. *J. Appl. Meteor.,* **43,** 170–181.

Klemp, J., J. Dudhia, and A. Hassiotis, 2008: An upper gravity-wave absorbing layer for NWP applications. *Mon. Wea. Rev.,* **136,** 3987–4004.

Knowles, N., M. D. Dettinger, and D. R. Cayan, 2006: Trends in snowfall versus rainfall in the western United States. *J. Climate,* **19,** 4545–4559.

Lim, K.-S. S., and S.-Y. Hong, 2010: Development of an effective double-moment cloud microphysics scheme with prognostic cloud condensation nuclei (CCN) for weather and climate models. *Mon. Wea. Rev.,* **138,** 1587–1612.

Lin, Y., and B. A. Colle, 2009: The 4–5 December 2001 IMPROVE-2 event: Observed microphysics and comparisons with the Weather Research and Forecasting model. *Mon. Wea. Rev.,* **137,** 1372–1392.

Lin, Y.-L., R. D. Farley, and H. D. Orville, 1983: Bulk parameterization of the snow field in a cloud model. *J. Climate Appl. Meteor.,* **22,** 1065–1092.

Lundquist, J., P. Neiman, B. Martner, A. White, D. Gottas, and F. Ralph, 2008: Rain versus snow in the Sierra Nevada, California: Comparing Doppler profiling radar and surface observations of melting level. *J. Hydrometeor.,* **9,** 194–211.

——, J. Minder, P. Neiman, and E. Sukovich, 2010: Relationships between barrier jet heights, precipitation distributions, and streamflow in the northern Sierra Nevada. *Water Resour. Res.,* **11,** 1141–1156.

Marwitz, J. D., 1983: The kinematics of orographic air flow during Sierra storms. *J. Atmos. Sci.,* **40,** 1218–1227.

——, 1987: Deep orographic storms over the Sierra Nevada. Part I: Thermodynamic and kinematic structure. *J. Atmos. Sci.,* **44,** 159–173.

Mattioli, V., E. R. Westwater, D. Cimini, J. C. Liljegren, B. M. Lesht, S. I. Gutman, and F. J. Schmidlin, 2007: Analysis of radiosonde and ground-based remotely sensed PWV data from the 2004 North Slope of Alaska Arctic Winter Radiometric Experiment. *J. Atmos. Oceanic Technol.,* **24,** 415–431.

Maurer, E., and C. Mass, 2006: Using radar data to partition precipitation into rain and snow in a hydrologic model. *J. Hydrol. Eng.,* **11,** 214–221, doi:10.1061/(ASCE)1084-0699(2006)11:3(214).

Medina, S., B. F. Smull, R. A. Houze, and M. Steiner, 2005: Cross-barrier flow during orographic precipitation events: Results from MAP and IMPROVE. *J. Atmos. Sci.,* **62,** 3580–3598.

——, E. Sukovich, and R. A. Houze, 2007: Vertical structures of precipitation in cyclones crossing the Oregon Cascades. *Mon. Wea. Rev.,* **135,** 3565–3586.

Mellor, G., and T. Yamada, 1982: Development of a turbulence closure model for geophysical fluid problems. *Rev. Geophys.,* **20,** 851–875, doi:10.1029/RG020i004p00851.

Milbrandt, J. A., and M. K. Yau, 2005a: A multimoment bulk microphysics parameterization. Part I: Analysis of the role of the spectral shape parameter. *J. Atmos. Sci.,* **62,** 3051–3064.

——, and ——, 2005b: A multimoment bulk microphysics parameterization. Part II: A proposed three-moment closure and scheme description. *J. Atmos. Sci.,* **62,** 3065–3081.

Minder, J. R., 2010: The sensitivity of mountain snowpack accumulation to climate warming. *J. Climate,* **23,** 2634–2650.

——, D. R. Durran, and G. H. Roe, 2011: Mesoscale controls on the mountainside snow line. *J. Atmos. Sci.,* **68,** 2107–2127.

Mlawer, E. J., S. J. Taubman, P. D. Brown, M. J. Iacono, and S. A. Clough, 1997: Radiative transfer for inhomogeneous atmospheres: RRTM, a validated correlated-k model for the longwave. *J. Geophys. Res.,* **102** (D14), 16 663–16 682.

Morrison, H., G. Thompson, and V. Tatarskii, 2009: Impact of cloud microphysics on the development of trailing stratiform precipitation in a simulated squall line: Comparison of one- and two-moment schemes. *Mon. Wea. Rev.,* **137,** 991–1007.

Neiman, P. J., G. A. Wick, F. M. Ralph, B. E. Martner, A. B. White, and D. E. Kingsmill, 2005: Wintertime nonbrightband rain in California and Oregon during CALJET and PACJET: Geographic, interannual, and synoptic variability. *Mon. Wea. Rev.,* **133,** 1199–1223.

——, F. M. Ralph, G. A. Wick, J. D. Lundquist, and M. D. Dettinger, 2008: Meteorological characteristics and overland precipitation impacts of atmospheric rivers affecting the West Coast of North America based on eight years of SSM/I satellite observations. *J. Hydrometeor.,* **9,** 22–47.

——, E. M. Sukovich, F. M. Ralph, and M. Hughes, 2010: A seven-year wind profiler–based climatology of the windward barrier jet along California's northern Sierra Nevada. *Mon. Wea. Rev.,* **138,** 1206–1233.

Parish, T., 1982: Barrier winds along the Sierra Nevada mountains. *J. Appl. Meteor.,* **21,** 925–930.

Pierce, D. W., and Coauthors, 2008: Attribution of declining western U.S. snowpack to human effects. *J. Climate,* **21,** 6425–6444.

Ralph, F. M., and Coauthors, 2005: Improving short-term (0–48 h) cool-season quantitative precipitation forecasting: Recommendations from a USWRP workshop. *Bull. Amer. Meteor. Soc.,* **86,** 1619–1632.

Reynolds, D., and A. Dennis, 1986: A review of the Sierra Cooperative Pilot Project. *Bull. Amer. Meteor. Soc.,* **67,** 513–523.

Rutledge, S. A., and P. V. Hobbs, 1983: The mesoscale and microscale structure and organization of clouds and precipitation in mid-latitude cyclones. VIII: A model for the ''seeder-feeder'' process in warm-frontal rainbands. *J. Atmos. Sci.,* **40,** 1185–1206.

Skamarock, W. C., and M. L. Weisman, 2009: The impact of positive-definite moisture transport on NWP precipitation forecasts. *Mon. Wea. Rev.,* **137,** 488–494.

——, and Coauthors, 2008: A description of the advanced research WRF version 3. National Center for Atmospheric Research Tech. Note NCAR/TN-475+STR, 113 pp.

Smith, B. L., S. E. Yuter, P. J. Neiman, and D. E. Kingsmill, 2010: Water vapor fluxes and orographic precipitation over northern California associated with a landfalling atmospheric river. *Mon. Wea. Rev.,* **138,** 74–100.

Stewart, R. E., J. D. Marwitz, J. C. Pace, and R. E. Carbone, 1984: Characteristics through the melting layer of stratiform clouds. *J. Atmos. Sci.,* **41,** 3227–3237.

Svoma, B. M., 2009: Trends in snow level elevation in the mountains of central Arizona. *Int. J. Climatol.,* **31,** 87–94, doi:10.1002/joc.2062.

——, 2011: El Niño–Southern Oscillation and snow level in the western United States. *J. Geophys. Res.,* **116,** D24117, doi:10.1029/2011JD016287.

Szyrmer, W., and I. Zawadzki, 1999: Modeling of the melting layer. Part I: Dynamics and microphysics. *J. Atmos. Sci.,* **56,** 3573–3592.

Tao, W.-K., and Coauthors, 2003: Microphysics, radiation and surface processes in the Goddard Cumulus Ensemble (GCE) model. *Meteor. Atmos. Phys.,* **82** (1–4), 97–137, doi:10.1007/s00703-001-0594-7.

Thériault, J., and Coauthors, 2012: A case study of processes impacting precipitation phase and intensity during the Vancouver 2010 Winter Olympics. *J. Hydrometeor.,* **27,** 1301–1325.

Thompson, G., R. M. Rasmussen, and K. Manning, 2004: Explicit forecasts of winter precipitation using an improved bulk microphysics scheme. Part I: Description and sensitivity analysis. *Mon. Wea. Rev.,* **132,** 519–542.

——, P. Field, R. Rasmussen, and W. Hall, 2008: Explicit forecasts of winter precipitation using an improved bulk microphysics scheme. Part II: Implementation of a new snow parameterization. *Mon. Wea. Rev.,* **136,** 5095–5115.

Tobin, C., A. Rinaldo, and B. Schaefli, 2012: Snowfall limit forecasts and hydrological modeling. *J. Hydrometeor.,* **13,** 1507–1519.

Unterstrasser, S., and G. Zängl, 2006: Cooling by melting precipitation in Alpine valleys: An idealized numerical modelling study. *Quart. J. Roy. Meteor. Soc.,* **132,** 1489–1508, doi:10.1256/qj.05.158.

Vicuña, S., E. P. Maurer, B. Joyce, J. A. Dracup, and D. Purkey, 2007: The sensitivity of California water resources to climate change scenarios. *J. Amer. Water Resour. Assoc.,* **43,** 482–498, doi:10.1111/j.1752-1688.2007.00038.x.

——, J. A. Dracup, and L. Dale, 2011: Climate change impacts on two high-elevation hydropower systems in California. *Climatic Change,* **109** (Suppl.), 151–169, doi:10.1007/s10584-011-0301-8.

Weber, B., D. Wuertz, and D. Welsh, 1993: Quality controls for profiler measurements of winds and RASS temperatures. *J. Atmos. Oceanic Technol.,* **10,** 452–464.

Wentz, F., 1995: The intercomparison of 53 SSM/I water vapor algorithms. Remote Sensing Systems Tech. Rep. on WetNet Water Vapor Intercomparison Project, 19 pp.

White, A. B., J. R. Jordan, B. E. Martner, F. M. Ralph, and B. W. Bartram, 2000: Extending the dynamic range of an S-band radar for cloud and precipitation studies. *J. Atmos. Oceanic Technol.,* **17,** 1226–1234.

——, D. J. Gottas, E. T. Strem, F. M. Ralph, and P. J. Neiman, 2002: An automated brightband height detection algorithm for use with Doppler radar spectral moments. *J. Atmos. Oceanic Technol.,* **19,** 687–697.

——, P. J. Neiman, F. M. Ralph, D. E. Kingsmill, and P. O. G. Persson, 2003: Coastal orographic rainfall processes observed by radar during the California land-falling jets experiment. *J. Hydrometeor.,* **4,** 264–282.

——, D. J. Gottas, A. F. Henkel, P. J. Neiman, F. M. Ralph, and S. I. Gutman, 2010: Developing a performance measure for snow-level forecasts. *J. Hydrometeor.,* **11,** 739–753.

Wisner, C., H. D. Orville, and C. Myers, 1972: Numerical model of a hail-bearing cloud. *J. Atmos. Sci.,* **29,** 1160–1181.